

Tutorial: a guide to diffusion MRI and structural connectomics

Received: 7 February 2023

Accepted: 9 July 2024

Published online: 4 September 2024

 Check for updates

Ittai Shamir^① & Yaniv Assaf^{1,2} 

Diffusion magnetic resonance imaging (dMRI) is a versatile imaging technique that has gained popularity thanks to its sensitive ability to measure displacement of water molecules within a living tissue on a micrometer scale. Although dMRI has been around since the early 1990s, its applications are constantly evolving, primarily regarding the inference of structural connectomics from nerve fiber trajectories. However, these applications require expertise in image processing and statistics, and it can be difficult for a newcomer to choose an appropriate pipeline to fit their research needs, not least because dMRI is such a flexible methodology that dozens of acquisition and analysis pipelines have been developed over the years. This introductory guide is designed for graduate students and researchers in the neuroscience community who are interested in integrating this new methodology regardless of their background in neuroimaging and computational tools. The guide provides a brief overview of the basic dMRI methodologies but focuses on its applications in neuroplasticity and connectomics. The guide starts with dMRI experimental designs and a complete step-by-step pipeline for structural connectomics. The following section covers the basics of dMRI, including parameters and clinical applications (apparent diffusion coefficient, mean diffusivity, fractional anisotropy and microscopic fractional anisotropy), as well as different approaches and models. The final section focuses on structural connectomics, covering subjects from fiber tracking (techniques, evaluation and limitations) to structural networks (constructing, analyzing and visualizing a network).

The connectome is the comprehensive structural connectivity diagram of the network of connections and elements that form the human brain¹. The importance of the connectome lies in uncovering the structural connectivity patterns of the brain and understanding the functional states that emerge from it. Several megaprojects have been initiated in the past decade aimed to unravel the brain's connectome, including the Human Connectome Project (HCP), the Blue Brain Project, the Human Brain Project (EU) and several others². The largest human brain magnetic resonance imaging (MRI) database, the UK Biobank, even includes in its MRI pipeline various connectivity measures, both structural and

functional. The HCP has taken the lead in the effort to map the wiring diagram of the human brain on the macroscopic scale, including long range connections (20–200 mm) between cortical regions on the scale of 1 mm³ (refs. 2–4).

Fiber tracking, or tractography, are terms used to describe the methods for inferring structural connectivity from the orientations of local nerve fibers. These orientations can be calculated from diffusion MRI (dMRI) experiments (or using more traditional methods, such as anterograde and retrograde tract tracing^{5,6}). In tractography nomenclature, the term 'tract' refers to the biological object modeled,

¹Department of Neurobiology, Faculty of Life Sciences, Tel Aviv University, Tel Aviv, Israel. ²Sagol School of Neuroscience, Tel Aviv University, Tel Aviv, Israel.
✉ e-mail: ittaisha@mail.tau.ac.il

either nerve tract, axon or fiber, while the term ‘track’ refers to the virtual object in the model, also known as a streamline. The resulting model of the brain’s fiber tracts, also known as a tractogram, includes all the three-dimensional (3D) white matter (WM) streamlines across the entire brain. Tractograms are often colored directionally.

One of the main challenges of connectivity research is accurately representing the tractography results so they can be quantified and compared both within and across subjects. Over the past decade, the use of graph theory tools for complex network analysis has become the state of the art in brain connectivity analysis⁷.

Pipeline overview

Different dMRI experiments use varying sets of imaging parameters, depending on the purpose of their experimental design. Common to all experimental designs is the need to reduce artifacts and signal loss by minimizing echo time, and to optimize the repetition time to achieve a reasonable signal-to-noise ratio (SNR), experimental time and brain coverage. Other varying parameters include pulse sequence-, gradient- and image-related parameters. For example, designing an experiment to measure mean diffusivity (MD) will probably necessitate fewer gradient directions than an experiment designed for tractography. Table 1 presents a summary of different dMRI experimental designs for a variety of advanced purposes.

HCP-style scan protocols are suitable for most dMRI applications. Although HCP-style scans might be considered excessive for applications such as MD, they are highly applicable for structural connectomics especially. Research MRI scanners typically have a stronger gradient system than clinical scanners, which results in better diffusion weighting and consequently better suitability for connectomics purposes. Scan protocols for both 3T and 7T MRI scanners are available at <https://www.humanconnectome.org/hcp-protocols>.

Generally, a structural connectomics pipeline for research includes the following main steps:

- Choose a dMRI method (according to research question)
- Perform a dMRI experiment (MRI scan protocol)
- Calculate fiber orientations (using either diffusion tensor imaging (DTI) or non-DTI methods)
- Calculate a tractogram (including tracts across the entire brain)
- Map the tractogram onto an atlas (cortical parcellation)
- Build the structural connectivity network (connectome)

Box 1 contains a stepwise procedure for following the processing pipeline (Fig. 1).

Many of these steps are computational calculations that need to be performed using appropriate software. We use ExploreDTI⁸ (<https://www.exploredti.com/>) to extract the structural connectome from raw dMRI data in MATLAB. While ExploreDTI is a well-established toolbox, many other pipelines exist for extracting structural connectomes using a variety of software programs, including, e.g., Mrtrix⁹, Tractoflow¹⁰, QSIprep¹¹ and Micapipe¹². All pipelines start with raw data extracted from a dMRI scan designed for connectomics and end with a connectivity matrix representing the structural connectome.

The next section describes the fundamentals of dMRI and then narrows in on dMRI for structural connectomics. It covers important concepts such as apparent diffusion coefficient, mean diffusivity, functional anisotropy and microscopic functional anisotropy, as well as different approaches to dMRI (the nonparametric approach and model-based parametric approaches).

The section on structural connectomics starts with fiber tracking (approaches, advanced techniques, criteria, evaluation and errors and limitations) then describes structural networks (constructing, analyzing and visualizing a structural network).

dMRI

dMRI is one of the most versatile MRI techniques both in its acquisition procedures and in its analysis pipelines, and has gained popularity over the past two decades not only in radiology but also in neuroscience. dMRI has opened a window into in-vivo tissue dynamics, becoming a microstructural imaging probe that measures the variability in properties, including tissue density and ordering.

dMRI has been used to explore the architecture and microstructural properties of both WM and gray matter (GM). Using various experiments and methodologies, discoveries relating to structure–function relations in the brain have been made^{13,14}. Some of these discoveries include rapid changes in several cognitive domains¹⁵, investigation of GM substructures using advanced dMRI techniques¹⁶ and multiple studies into the opportunities and remaining challenges in structural connectomics^{17–19}. Thanks to its enhanced contrast, dMRI holds valuable information with multiple clinical applications in radiology and neurology^{5,6,13,14}.

The dMRI pulse sequence, called pulsed gradient spin echo (PGSE), consists of a normal spin echo sequence plus two magnetic gradient

Table 1 | dMRI experimental designs for different advanced purposes

Purpose	Focus of experimental design	Refs.
1 MD/FA clinical research	While in the past the notion was that a set of six gradient directions was optimal for DT MRI, studies have since concluded that robust estimation of FA requires >20 gradient directions, and MD and tensor orientation require >30 gradient directions. Typically, $b = 1,000 \text{ s/mm}^2$, but b -values in the range of 700–1,200 s/mm^2 are appropriate	107
2 Neuroplasticity	Accurate registration is highly important when examining neuroplasticity. The MRI datasets must be precisely spatially aligned to avoid the loss of structural features. To accurately explore and interpret changes in neuroplasticity, the chosen brain atlas must be transformed to the space of the individual subject brain, while leaving the MRI dataset intact	29,30
3 Microstructure exploration	Studies suggest that high quality dMRI can be produced at 7T using advanced techniques adapted for high magnetic fields. The resulting images have isotropic resolutions of up to 800 μm , suitable for exploration of microstructural properties of fiber architectures. Similar studies can be conducted at 3T, however longer acquisition times are required	64
4 Axon diameter	To achieve a robust proxy of axonal diameter information across the brain, high gradient strength is needed. The different techniques, including AxCaliber, COMMIT and ActiveAx, all necessitate applications of high and ultra-high gradients, with Gmax > 1,200 mT/m and higher	50,53,62,63
5 GM	While MD and FA exhibit little variability across the cortical layers, the fODF exhibits an ability to delineate the cortical layers. Image resolution is key to layer delineations according to the direction of aligned groups of fibers	66
6 Functional diffusion	Fast acquisition is key in diffusion-weighted functional MRI, which uses highly sensitized diffusion imaging to explore the diffusion response function that precedes the hemodynamic response function explored using functional MRI	108–111
7 Fiber tracking	Studies recommend using HARDI with $b = 3,000 \text{ s/mm}^2$, pending on SNR, to provide the highest angular resolution. However, more realistic b -values in the range of 1,000–3,000 s/mm^2 are also appropriate. Studies also recommend acquiring >45 gradient directions to help avoid issues with imperfections in gradient uniformity and meet SNR requirements	27,65
8 Connectomics	To accurately map connections between cortical regions, the anatomical stopping criterion in tractography must allow streamlines to enter cortical GM. Furthermore, choice of cortical parcellation dictates the level of detail of the resulting brain network	7

BOX 1

Processing pipeline for performing structural connectomics

The processing pipeline for structural connectomics is shown in Fig. 1 and described below.

1. Perform a dMRI scan designed for structural connectomics. HCP-style scan protocols are suitable for structural connectomics applications of dMRI. Detailed scan protocols for both 3T and 7T MRI scanners are available at <https://www.humanconnectome.org/hcp-protocols>.

Another detailed example protocol can also be found in a recent structural connectomics study¹⁷, using a standard DWI sequence, with the following parameters: $\Delta/\delta=60/15.5$ ms, $b_{\text{max}}=5,000$ (0, 250, 1,000, 3,000 and 5,000) s/mm², with 87 gradient directions, FoV 204 mm, maxG=7.2, TR=5,200 ms, TE=118 ms, $1.5 \times 1.5 \times 1.5$ mm³, 128×128×94 voxels. Each subject was scanned on a 3T Magnetom Siemens Prisma (Siemens) scanner with a 64-channel RF coil and gradient strength of up to 80 mT/m at 200 mT/s.

Before starting the analysis, note that the DWI images and the cortical atlas must be spatially aligned, preferably in a standardize brain space, such as the MNI space (named after its origin in the Montreal Neurological Institute). This step can be efficiently completed using SPM12 (<https://www.fil.ion.ucl.ac.uk/spm/software/spm12/>) or any other software for image registration.

2. The raw data from a dMRI scan comes in the form of Digital Imaging and Communications in Medicine (DICOM) images. Convert the DICOMs into 3D images using dcm2nii (<https://www.nitrc.org/projects/dcm2nii/>).
3. DICOM conversion results in a 3D NIfTI (Neuroimaging Informatics Technology Initiative) image, and two files representing the *b*-values and *b*-vectors. Convert the *b*-val and *b*-vec files to a *b*-matrix text file using a conversion plugin. If needed, the *b*-matrix is reordered so zero values are moved to start using either sort or shuffle plugin. The following steps are then completed using ExploreDTI⁸ (<https://www.exploredti.com/>).

4. Use the shuffled NIfTI and *b*-matrix files to calculate the DTI MATLAB file using the conversion to raw data plugin. Parameters are chosen according to data: image size, voxel size, etc.
5. Load the converted DTI file. The image view is color-coded according to directionality.
6. Check that the gradient directionality of known elements is accurate. To do this, load the axis and draw tools, and draw the tensors in a selected region of interest, such as the corpus callosum. If accurate, the corpus callosum should appear in red due to its left-right fiber orientation.
7. To improve SNR, denoise the image by correcting for subject motion and other distortions using the appropriate plugin. The image should appear visibly cleaner, particularly in regions outside the brain.
8. Using the correct DTI file and the appropriate plugin, calculate whole-brain tractography. The calculation necessitates choosing the fitting parameters according to the image data and user needs, for example using either the DTI default or CSD. This process may take several minutes to complete.
9. View the resulting fiber tracts by loading the resulting MATLAB file containing the tracts.
10. The whole-brain tractogram can be viewed and further assessed by rotating the axes in 3D.
11. Select an appropriate atlas (parcellation) for constructing a network from the tractogram.
12. Build the tract connectivity matrix across the selected atlas using the network analysis tools plugin.
13. The resulting connectivity matrix represents the structural connectome, which can be analyzed for various network features using the Brain Connectivity toolbox (<https://sites.google.com/site/bctnet/>), or any other software for network analysis and visualization.

pulses. The first gradient pulse occurs after the 90° radio frequency (RF) pulse. For the second gradient pulse, the direction of the magnetism is reversed; it occurs after the 180° RF pulse (Box 2). A dMRI experiment is defined by multiple parameters, including parameters relating to the pulse sequence and more specifically those relating to the gradients applied, as well as parameters relating to the image acquisition. Table 2 summarizes the main parameters in a dMRI experiment.

One of the most basic and robust parameters dMRI measures is the apparent diffusion coefficient or mean diffusivity (for more on measuring the diffusion coefficient using dMRI, see Box 2).

dMRI has become a popular *in vivo* imaging technique thanks to its highly sensitive ability to measure the displacement of water molecules that typically move a few micrometers during an experiment. dMRI is sensitive not only to the magnitude of the displacement of water molecules, but also to the directionality of this displacement (for more on the subject, see Box 3). In the simplest case, this image shows the degree to which water molecules are displaced in each voxel. The output image of dMRI is known as a diffusion-weighted image (DWI), which represents the measured displacement of water molecules. An inverse relationship exists between the measured diffusivity of water molecules and the obtained DWI signal. Short displacement range and low diffusivity of water molecules results in a strong DWI signal, and long displacement range and high diffusivity result in a weak DWI

signal²⁰. For example, because water molecules experience higher diffusivity in cerebral spinal fluid (CSF) than in cerebral WM, in the resulting image CSF would be represented by a lower DWI signal intensity than WM (Fig. 2a). Thanks to its enhanced contrast, dMRI holds valuable information with multiple clinical applications in radiology and neurology^{5,6,13,14}.

dMRI fundamentals

Several extractable dMRI parameters have demonstrated sensitivity toward tissue microstructure dynamics, offering various neuroimaging applications. The major extractable parameters are described below.

ADC. The apparent diffusion coefficient (ADC) represents the calculated diffusion coefficient of water molecules in the direction of the applied gradients. In the most basic form, ADC is extracted from DWI images as the log average from three perpendicular DWI acquisitions.

A direct relationship exists between the measured diffusivity of water molecules and the calculated ADC value. In an ADC image, a strong signal represents a long displacement range and a high diffusion coefficient, and a low signal represents short displacement and a low diffusion coefficient. ADC values differ greatly between tissues depending on their tissue microenvironments: CSF has higher ADC values than cerebral GM, since CSF is a fluid with a less restricting extracellular structure. GM in

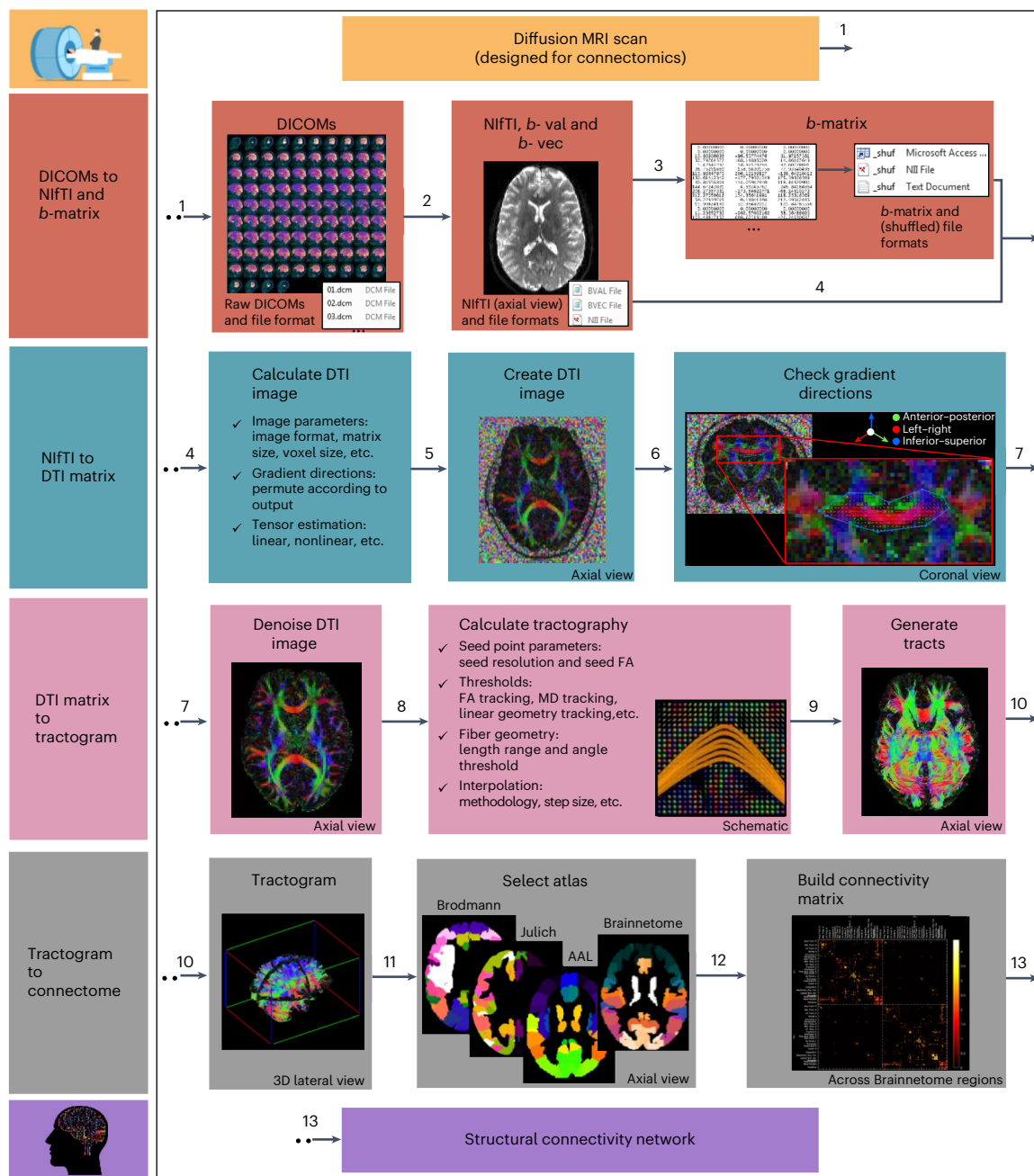


Fig. 1 | The processing pipeline for performing structural connectomics. Steps 1–13 are described in detail in Box 1.

turn has higher ADC values than WM, since WM has a more restricting extracellular structure due to its myelinated axonal fiber content and high tissue packing compared with the neuronal cell bodies and dendrites in GM. Typical value ranges are as follows: WM, $0.6\text{--}1.05$ ($10^{-3}\text{ mm}^2/\text{s}$); GM, $1.05\text{--}2.4$ ($10^{-3}\text{ mm}^2/\text{s}$); and CSF, $2.4\text{--}4.4$ ($10^{-3}\text{ mm}^2/\text{s}$) (Fig. 3a).

One of the first clinical applications of dMRI was the early detection of cerebral ischemia and stroke using ADC images. ADC values in the affected tissue tend to decrease because of a cascade of events involving cell swelling^{21–25}. While ADC is a difficult parameter to quantify and interpret, this clinical application of dMRI has opened the door to diagnostic imaging of suspected stroke patients and validated its use as a microstructural probe²⁶.

Since ADC is a difficult parameter to quantify and interpret, and since more useful and applicable parameters can be extracted from DTI, it is rarely used nowadays. Some of the more applicable parameters include MD and fractional anisotropy (FA) (discussed below)^{27,28}.

MD. MD represents the average apparent diffusion coefficient of water molecules across three perpendicular directions of movement. MD is comparable to ADC in concept, but it is calculated from the diffusion tensor (DT), rather than from the DW image (Box 3). As a result, MD exhibits rotational invariance and provides a more accurate measure for estimation of diffusion coefficients, particularly in regions with high anisotropy. In other words, DTI provides a more robust ground for evaluating the average diffusion value. MD exhibits characteristic values of $\sim 0.7\text{--}0.8$ ($10^{-3}\text{ mm}^2/\text{s}$) in WM and values >0.8 ($10^{-3}\text{ mm}^2/\text{s}$) in GM^{29,30} (Fig. 2b,c).

MD is considered an excellent parameter for exploring long lasting structural remodeling of neural tissue, also known as neuroplasticity. Neuroplasticity entails a sequence of cognitive and physiological processes with hallmark strengthening and weakening of synaptic activity between neurons in specific task related regions³¹. MD values change following remodeling of relevant regions. For example,

spatial learning induces an increase in synaptic activity in parts of the hippocampus³². Studies have shown that this synaptic activity colocalizes with glial cell morphological remodeling and swelling, a common process that accompanies synaptic plasticity³³. This swelling leads to a subtle decrease in MD of 1–5%, which has been attributed to an increase in cell density, and which results in a restriction of the movement of water. This phenomenon is not only highly sensitive and specific, but also persistent over a wide range of time scales, from minutes to days and weeks following the task^{15,29,30,32–34}.

Many questions still stand to be addressed relating to the time course of MD changes, the mechanisms behind these changes and the difference in mechanisms between short- and long-term neuroplasticity. Despite these open questions, multiple studies have revealed regional changes in MD values within minutes of performing cognitive tasks in different cognitive domains. These changes entail a decrease in MD values in multiple brain regions following tasks such as object recognition, spatial navigation, motor sequence learning and new lexical learning^{15,29,30,32–34}. Different neurological conditions also exhibit changes in MD, including pathologies such as stroke, Alzheimer's disease and epilepsy^{21–23,35,36} (for more on MD, see Supplementary Note). These studies highlight the ability of MD to explore structural neuroplasticity in an unprecedented way and its potential as a microstructural probe for examining the effects of learning and cognition. While MD is rotationally invariant, other dMRI parameters relate directly to its directionality (discussed below).

FA. FA represents the degree of directionality or tendency of water molecules to diffuse in a single direction. High anisotropy is represented by a more elliptical and directional DT (as shown in Box 1), due to higher diffusivity in the axial direction than in the radial directions. FA values are unitless and range between 0 and 1, where 0 represents complete isotropy or uniformity in directionality, and 1 represents complete anisotropy or directionality. For example, CSF exhibits low FA values because water molecules within its microenvironment are free to move in all directions equally. WM on the other hand exhibits higher FA values, since water molecules within its microenvironment move more freely in the direction of its axonal fibers, compared with the more restricted movement in the perpendicular direction. FA exhibits characteristic values of ~0.1–0.2 in GM and values >0.3 in WM. These values, also known as eigenvalues, do not, however, give any information about the primary direction. The direction information is present in the eigenvectors. After DTI modeling, FA maps are often visualized according to the DTI color coding, in a way that assigns a color to each direction: left–right: red; anterior–posterior: green; inferior–superior: blue (Fig. 3b,c).

FA provides a quantitative measure that has advanced the exploration of the healthy neuroanatomy of WM, its development and its degeneration due to both aging and various degenerative clinical conditions¹⁶. FA was exceptionally popular in the early days of DTI, but its use has since become limited due to inherent artifacts in areas of heterogeneous fiber orientation and organization, such as crossing

BOX 2

Measuring the diffusion coefficient

The mobility of water molecules varies between different brain tissues, depending on the freedom of movement allowed by the tissue microenvironment. The neuronal microenvironment includes both the space within the cells (intracellular) and outside them (extracellular), or more specifically in relation to an axon (intra-axonal and extra-axonal spaces). The freedom of movement of water within these spaces is highly influenced by the biological microstructure of the tissue, including the levels of tissue density and fiber organization^{5,6,32}.

To simplify the equation representing signal decay in a PGSE experiment, water diffusion within the measured area is assumed to have a normal Gaussian distribution^{5,118–120}.

The relationship between signal decay and the summed PGSE parameters to a common index, called the *b*-value, can then be represented by the Stejskal–Tanner equation⁴¹:

$$E(q) = e^{-bD} \quad (1)$$

where $b = q^2 D (\Delta - \frac{\delta}{3})$ and $q = \gamma \delta G$ (2), (3) γ is the gyromagnetic ratio of magnetic to angular momentum of a water particle. Δ is the diffusion time, the time between the application of the two gradients; δ is the diffusion gradient duration; G (or g) is the diffusion gradient amplitude and direction; D is the diffusion coefficient, in either scalar or tensor form.

The image below shows a PGSE sequence, including two 90° gradient pulses separated by an 180° pulse (a), additional gradients applied after each pulse (b) and the obtained signal (c), including the short response after the 90° pulse, known as free induction decay (FID), and the signal echo. In the image, δ , G and Δ are as defined above; FID is the free induction decay, TE is the echo time and TR is the repetition time (adapted from ref. 13).

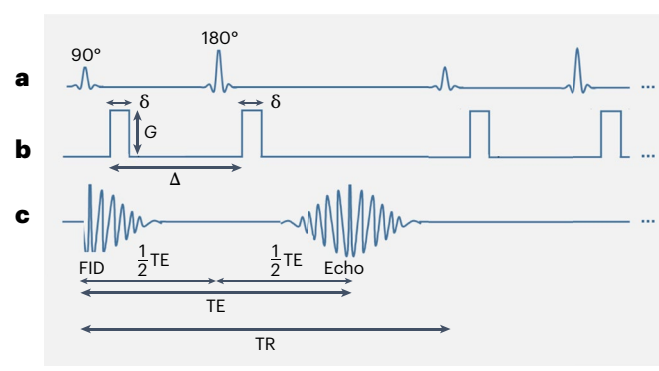


Image adapted with permission from ref. 13, Elsevier.

dMRI image acquisition

The ‘*b*-value’, a term originated by Le Bihan¹⁰⁸, is a factor calculated from the chosen gradients and their timing (G and δ). The *b*-value determines signal sensitivity to molecular motion and the resulting strength of signal attenuation. Higher *b*-values, which result in stronger attenuation, are reached using larger gradient amplitudes (G), longer gradient durations (δ) or longer durations between pulses (Δ or Δ). The typical range of *b*-values is 0–5,000 s/mm², with more commonly used values of up to 1,000 s/mm².

There is no single optimal *b*-value; this parameter can be optimized experimentally such that signal attenuation is minimized while balancing sensitivity and specificity. A useful rule-of-thumb is that the product of the *b*-value and the apparent diffusion coefficient (see ‘Parameters and clinical applications’) should approximately equal 1.

(continued from previous page)

Various resulting images can be seen below, including images comparing three different gradient directions across the same axial slice, and images comparing several different b -values (right) (a), including 5 s/mm^2 (b), 1,000 s/mm^2 (c), 2,000 s/mm^2 (d) and

4,000 s/mm^2 (e), in a single gradient direction: inferior–superior. Images seen from different viewpoints: coronal (left column), sagittal (mid column) and axial (right column).

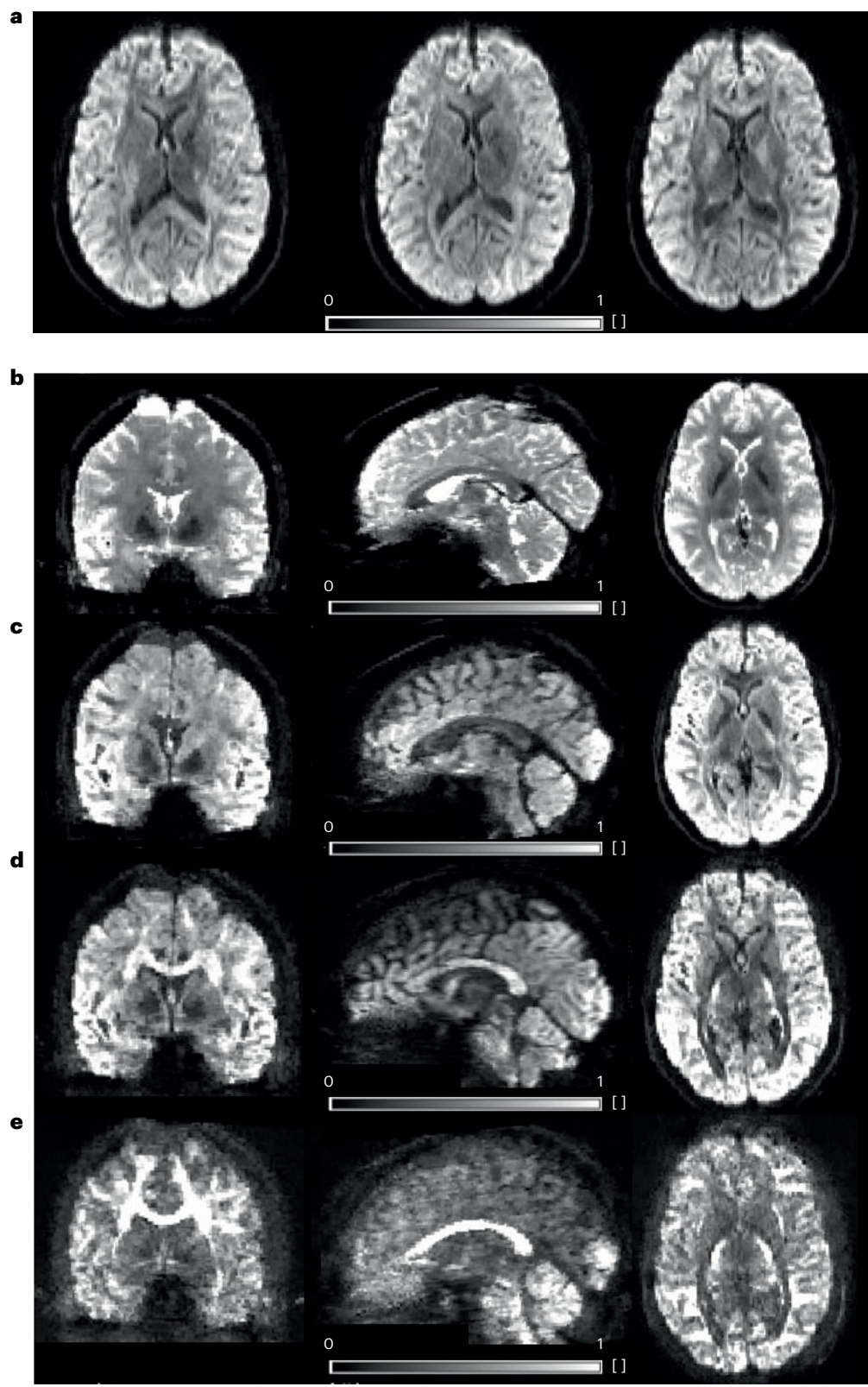


Table 2 | dMRI experiment parameters

Parameter	Symbol	Units	Definition
Pulse sequence parameters:			
1	Repetition time (time to repetition)	TR	ms
2	Echo time (time to echo)	TE	ms
3	Diffusion time	d or Δ	ms
4	Acquisition time	TA	min or h
5	Sound-to-noise ratio	SNR	–
6	b -value	b	s/mm ²
6a	b -value shells	n	–
Gradient parameters			
7	Gradient	G , g or maxG	mT/m
8	Gradient duration	δ	ms
9	Gradient directions	–	–
Image parameters			
10	Image size	–	Number of voxels
11	Resolution	–	mm ³
12	Field of view	FoV	mm or cm
13	Matrix size	–	–
14	Number of slices	–	–

fibers, as well as difficulties in its interpretation. FA sensitivity to anisotropy in cellular structure is limited by its sensitivity to orientation dispersion due to averaging of multiple fiber orientations within a single voxel^{17–19}. In recent years, other models have overcome these issues and become the first line of analysis to extract similar information to FA (discussed below).

To overcome the inherent pitfalls in FA calculation, an alternate acquisition and analysis pipeline was developed to introduce microscopic FA (microFA). MicroFA overcomes the partial volume effect (PVE) (discussed below) limiting the sensitivity of FA to complicated tissue organization, e.g., WM fiber dispersion. Calculation of microFA involves additional considerations for microstructural features, such as the shape and orientation of structures within a voxel, achieved through advanced modeling techniques that attempt to capture finer details.

MicroFA uses a modified version of PGSE to quantify diffusion anisotropy independently of the orientation dispersion using powder averaging, which involves calculating the mean dMRI signal across evenly distributed directions in a sphere. Substantial differences between FA and microFA are evident in regions with crossing fibers and intersections between large fiber tracts, where FA is low and microFA is high. MicroFA has also demonstrated the clinical application of differentiating between types of brain tumors, for example, meningiomas and glioblastomas. The disparity between FA and microFA in meningiomas indicates that this tumor contains disordered anisotropic structures, further establishing the role of microFA as a complementary tool to FA^{37–40}.

Different approaches to dMRI

Despite the popularity of dMRI, it is evident that some aspects of the analysis need to be revisited, as they model the tissue in a non-optimal way. The most fundamental conceptual pitfall involves the name of the method. dMRI does not directly measure the diffusion of water molecules, but instead measures their displacement.

Only in special physical conditions the displacement can be linked to diffusion.

dMRI was developed by Stejskal and Tanner⁴¹ under the assumption that the displacement of water molecules is Brownian and that the values would have a Gaussian distribution. However, the displacement of water molecules in biological tissues is often restricted by membranes and other cellular structures and therefore does not always follow this assumption. This phenomenon has been demonstrated experimentally: water motion in the brain as measured by ADC was found to be dependent on the probing time of the diffusion gradients. If the water motion had Gaussian distribution, there should be no dependency. In other words, ADC values level out at higher b -values, following the linear part of the signal in lower b -values that corresponds to Gaussian behavior¹³. Deviations from Gaussian diffusion indicate that the modeling basis of dMRI does not entirely capture the complexity of water motion in the brain and thus it needs to be further developed. Furthermore, values in dMRI are averaged per voxel, generating volumetric averaging across brain tissues in an effect known as the PVE. As a result, image resolution still limits the ability of the microstructural probe to investigate brain tissue in techniques such as DTI¹³ (Table 2).

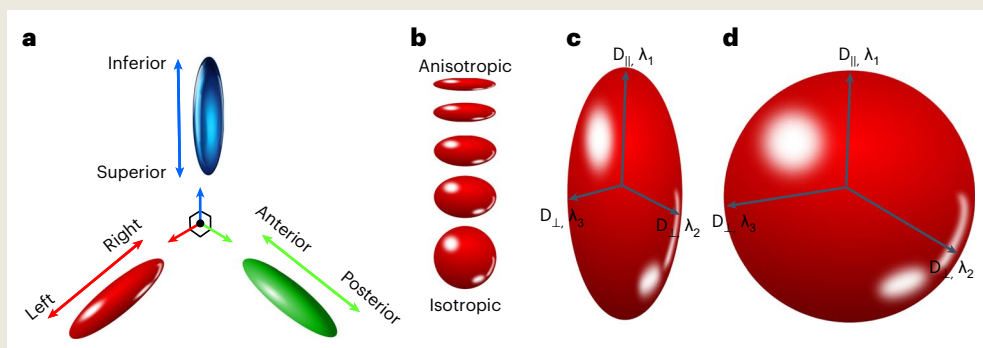
Multiple approaches and solutions have been developed for overcoming the conceptual and methodological limitations of dMRI. One elegant, model-free approach uses the q -space, representing the reciprocal spatial domain instead of the spatial frequency domain (also known as k -space), by using a fast Fourier transform of the diffusion signal decay^{42,43}. While use of q -space is elegant and theoretically straightforward, it necessitates intricate experimental conditions, such as a strong gradient system, that often cannot be met in clinical MRI scanners but only in scanners for research purposes^{42,43}.

Over the years, scientific efforts have been made to develop suitable non-DTI methods. These methods are based on either the nonparametric (model-free) approach, or the parametric approach, including biophysical models for estimating both axon density and

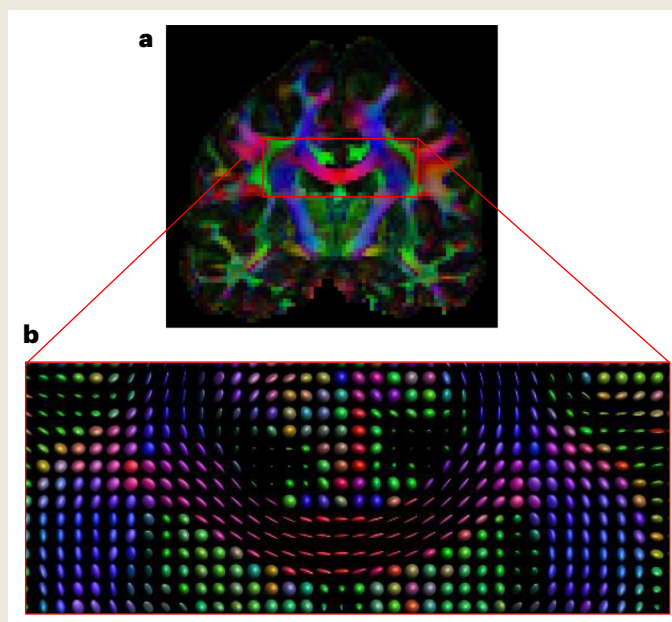
BOX 3**DTI**

The dMRI signal depends not only on the magnitude of the applied gradients, but also on the direction in which they are applied. The generated gradient can be applied in any direction, leading to sensitivity to diffusion processes that occur along a specific direction. Regions with high apparent diffusion anisotropy, or high motional directionality, as in neural fibers, show differential signal attenuation based on the direction of the applied gradient. DTI is a model that was developed in the early 1990s generalizing dMRI and quantifying and visualizing this phenomenon^{120–122}. Its development originated from the discovery that gradients that are applied in different directions result in different image contrasts, suggesting that the displacement of water molecules is not necessarily directionally uniform or isotropic. DTI expands the single diffusion value to a full quantification of DT in a rotationally invariant manner^{123,124}. The image below shows tensor color where (a) is tensor color coding

according to diffusion directions. The full directionality of diffusion in DTI is represented by a matrix called a DT. The eigenvectors of the DT represent the directions of the diffusivity, and its eigenvalues represent the diffusion values in the corresponding directions. The DT is commonly represented visually by an ellipsoid, made up of three perpendicular vectors, including the main axis in the principal direction of diffusion and two minor axes. Diffusivity in the principal direction of an ellipsoid is called axial diffusivity, and diffusivity perpendicular to the principal direction is called radial diffusivity. The image below shows the tensor shape where (b) degrees of diffusion directionality, ranging from high directionality, also known as anisotropy (a more elliptical tensor shape), to low directionality, also known as isotropy (a rounder tensor shape) and (c,d) primary tensor directions of both axial ($D_{||}$) and radial (D_{\perp}) diffusivity.

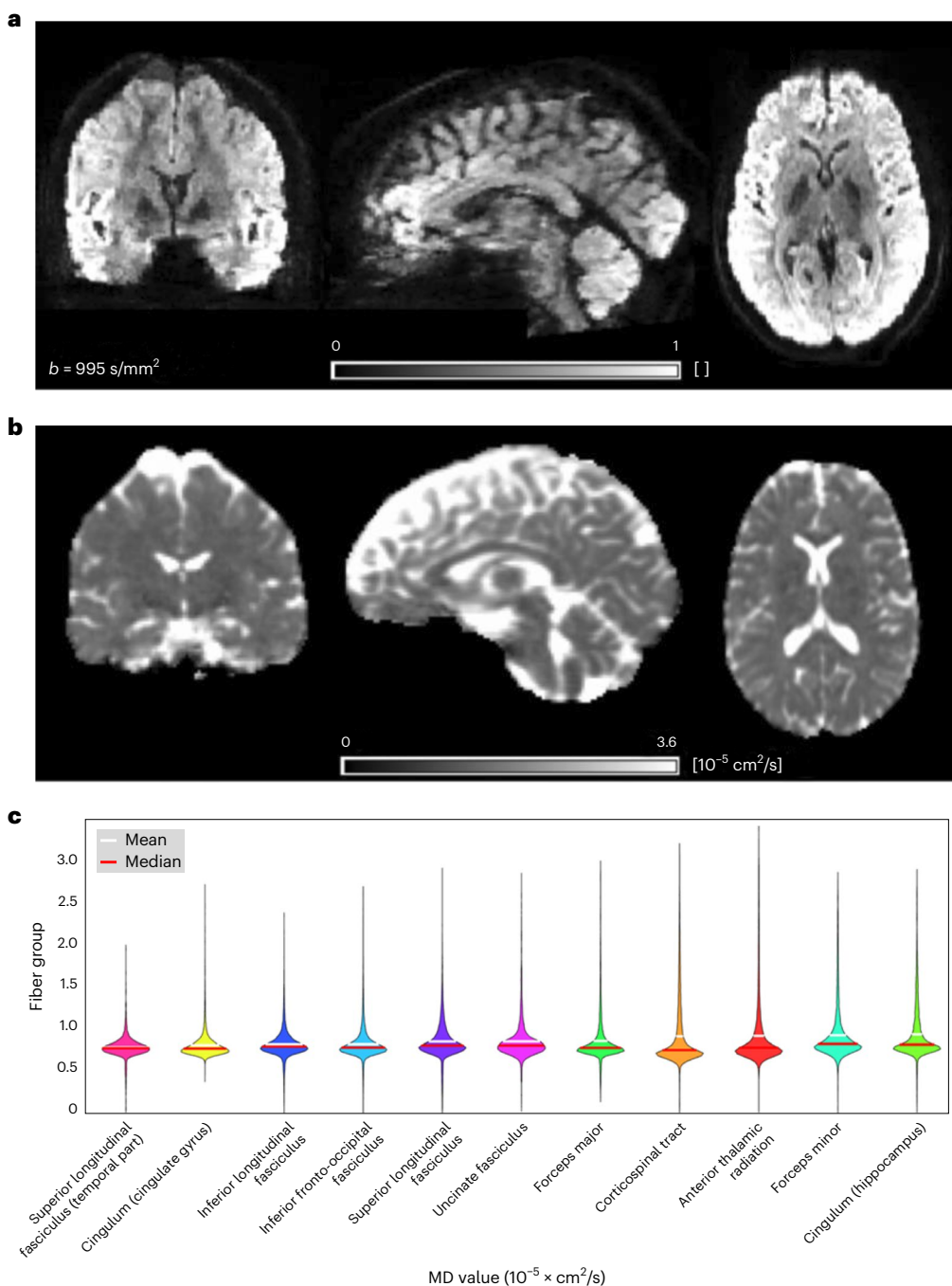
**DT ellipsoid shape and color**

An image showing a coronal view of a colored tensor field (a), shown across the corpus callosum (b).

**DT field**

diameter. Each approach necessitates a different set of assumptions and methods, as well as a different combination of scan parameters, such as b -values and gradient directions.

The nonparametric approach: DKI. One of the leading nonparametric approaches is diffusion kurtosis imaging (DKI), which was developed to overcome the Gaussian displacement assumption and better describe



the complex actuality of intracellular and extracellular *in vivo* environments^{44–46}. This heterogeneous non-Gaussian behavior of diffusion becomes more noticeable with higher b -values or stronger gradients and longer echo times. To deal with these deviations, DKI uses a statistical measure called kurtosis (K) that measures the deviation from a Gaussian distribution, or ‘tailedness’ of a distribution. When $K = 0$, no deviation exists, and the distribution is considered Gaussian. Negative kurtosis ($K < 0$) indicates a ‘fatter’ and less ‘peaked’ distribution than a Gaussian one, and positive kurtosis ($K > 0$) indicates a ‘slimmer’ and more ‘peaked’ distribution. Kurtosis is often measured in multiple directions, resulting in a fourth order tensor with several components, which are averaged into a rotationally invariant alternative value called mean K . Most biological tissues are better characterized by ($K > 0$), since water molecules

within them experience limited motion due to constraints on their ability to displace. Studies using DKI have shown its contribution as an independent and complementary dMRI technique, revealing improved WM characterization and increased sensitivity and specificity in evaluation of pathologies, disease progression and response to treatment^{44,45}.

The parametric approach: biophysical models. Biophysical models exploit the deviations of diffusivity from the Gaussian behavior to model various tissue components using multiple b -values. Models necessitate a set of assumptions and approximations regarding tissue geometry, scan parameters and the expected displacement of water molecules during the scan. These assumptions and approximations allow for a mathematical simplification of the signal decay. In such

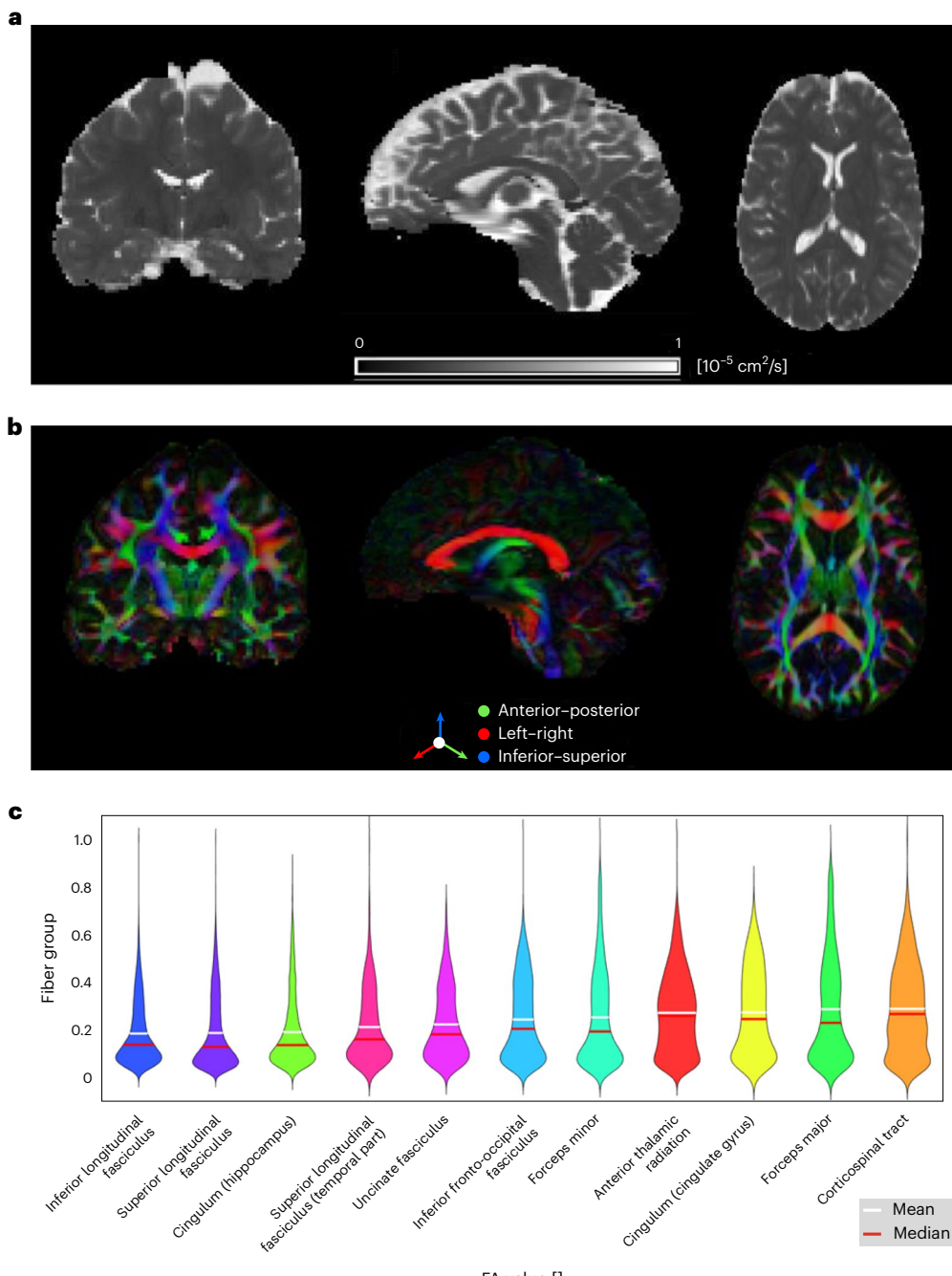


Fig. 3 | ADC and FA. ADC images in a single direction (a), and FA images (b), including the distribution of FA values across various fiber groups in the brain (c). Both types of images are seen from different viewpoints: coronal (left column), sagittal (mid column) and axial (right column).

approaches, the tissue is assumed to be composed of several, distinct, biophysical components, with or without interactions (exchange) between them. For example, GM tissue can be modeled by a set of spheres (representing cells) and nonorganized cylinders (representing neural processes). In addition, extracellular space can be modeled by Gaussian diffusion at first approximation. In WM, it is possible to add other factors as the neuronal processes (axons) are packed, introducing other parameters such as packing density and diameter distribution.

Regarding axon density estimation, neuronal tissue can be modeled as a combination of different components based on their level of water diffusivity:

- The first component displays restricted diffusion, which models the limited permeability of myelinated neural cells in WM.

Restricted diffusion is the main cause for disturbances in the Gaussian nature of diffusion of water molecules and therefore exhibits non-Gaussian diffusion properties

- The second component displays hindered diffusion, which models the more Gaussian-like diffusion properties of GM, due to the less constrained diffusion properties of unmyelinated neural cell bodies. Hindered diffusion can be expressed mathematically using the classic DTI formula due to its Gaussian-like diffusion properties
- The third component displays isotropic diffusivity, which models free water molecules in CSF outside fiber populations
- The fourth component, or rather modeling consideration, is the presence of branching, overlapping and crossing fiber populations

Various multiparameter biophysical models use these components to try to capture the axon density at different levels of detail and simplification. Mathematically, introducing many parameters to a modeling or fitting routine can lead to overfitting, as the number of measured data samples is limited. Therefore, trying to capture and model all tissue compartments comprehensively at the same time is not recommended. Instead, any suggested model needs to focus on the specific tissue compartment it wishes to model.

- The composite hindered and restricted model of diffusion (CHARMED) models the dMRI signal as a linear combination of the signal decays of hindered and restricted diffusion components, multiplied by their corresponding volume fractions⁴⁷
- Neurite orientation dispersion and density imaging (NODDI) models the structure and direction of axons and dendrites using three components, including intracellular, extracellular and CSF, and utilizing mathematical simplifications such as the orientation-dispersed cylindrical assumption⁴⁸
- Distribution of anisotropic microstructural environments in diffusion-compartment imaging (DIAMOND) models the dMRI signal using three components, including restricted, hindered and isotropic diffusion, in a hybrid model of the tissues that is both biophysical and statistical⁴⁹

Regarding axon diameter estimation, dMRI has also been demonstrated sensitivity to axon diameter under certain experimental conditions^{28,50–52}. While exact and absolute estimation of axon diameters is probably unattainable, some models offer a robust proxy of diameter information using dMRI. AxCaliber was the first biophysical model developed to estimate the axonal diameter distribution, followed by ActiveAx, AxCaliber3D, ActiveAxADD, convex optimization modeling for microstructure informed tractography (COMMIT), AMICO, axonal spectrum imaging (AxSI) and others^{53–61}.

AxCaliber is an expansion of CHARMED that incorporates the axon diameter from histology as an additional factor in the model. Instead of the predefined distributions, AxCaliber uses a gamma distribution function to fit the axon diameter distribution^{38,50,52,62}. Use of a gamma function increases model complexity by introducing additional parameters for evaluation that necessitate additional optimization methods.

Originally, AxCaliber was implemented in a simplified way by imposing acquisition to measure diffusion perpendicular to fiber orientations. This simplification caused decreased sensitivity toward small axons and a limited ability to separate hindered and restricted components⁵⁰. The method has since been expanded to 3D in a method named AxSI, increasing its applicability in connectomics. AxSI estimates axon diameters across all fiber systems and enables *in vivo* explorations of information transfer mechanisms across the brain⁶² (Fig. 4a). Other methods, including COMMIT⁵³ and ActiveAx⁶³, incorporate dispersion to increase the accuracy of the estimated axon diameter distribution.

Essentially, dMRI acquisition techniques can be categorized as either single- or multishell. Single-shell acquisition involves a single nonzero b -values, and multishell acquisition involves multiple nonzero b -values. Single-shell acquisition is commonly used for basic DTI analysis or for high angular resolution diffusion imaging (HARDI), in experiments where $b = 1,000 \text{ s/mm}^2$, for example); multi-shell is used for HARDI (for solving crossing fibers, for example, refs. 64,65), DKI, and biophysical models, such as CHARMED and AxCaliber.

Structural connectomics

Tractography has propelled the field of imaging-based structural connectomics, which involves the whole-brain study of neural connections across the brain⁶⁶. Since its origination, a variety of techniques and approaches have been offered for modeling nerve tracts from dMRI⁵.

Different approaches to tractography

All tractography techniques involve reconstructing fiber track streamlines following the local principal directions estimated from dMRI (Fig. 5). Historically, DTI was used for tractography using methods such as fiber assessment by continuous tracking (FACT). FACT is a classic tractography method that uses the DT field and then reduces it to vectors representing the ‘strongest’ and most likely vector-to-vector directional connections. Techniques such as FACT use DTI modeling to estimate the tracts in a deterministic fashion.

More modern applications use non-DTI methods for tractography (see HARDI below). Multifiber models are more commonly used today, including tracking based on orientation distribution function

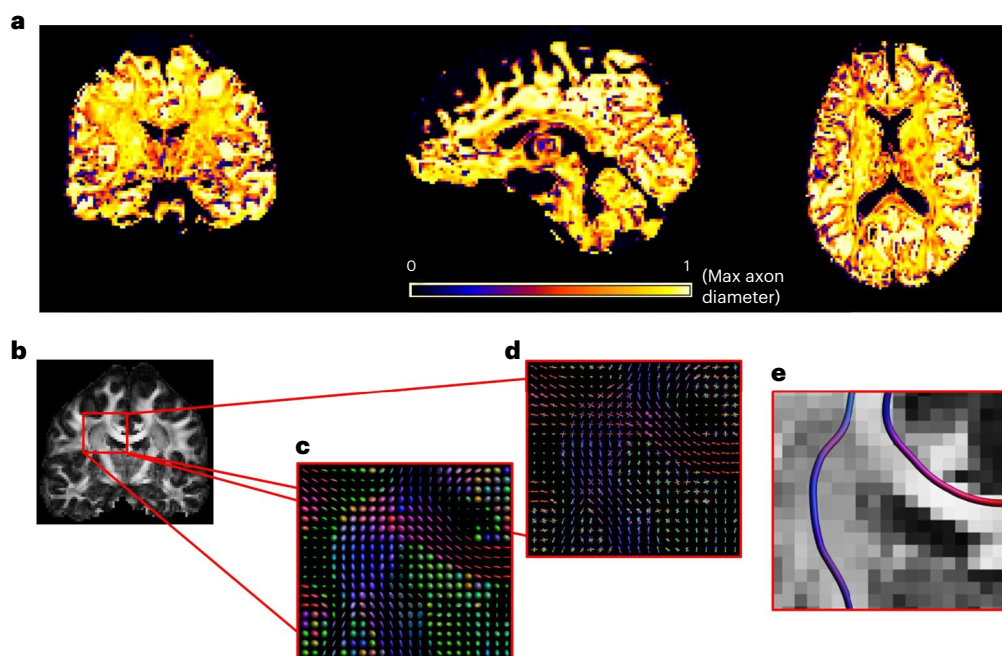


Fig. 4 | Axon diameter and tractography. a, Axon diameter (AxCaliber) images, representing the relative measured axon diameter values across the WM, seen from different viewpoints: coronal (left column), sagittal (mid column) and axial (right column). b–e, Tractography: FA map (b), and DT fields across a chosen ROI,

including DTI tensor field (c) and HARDI tensor field (d), and two reconstructed streamlines (e): one streamline in the corticospinal tract (left) and another streamline in the corpus callosum (right).

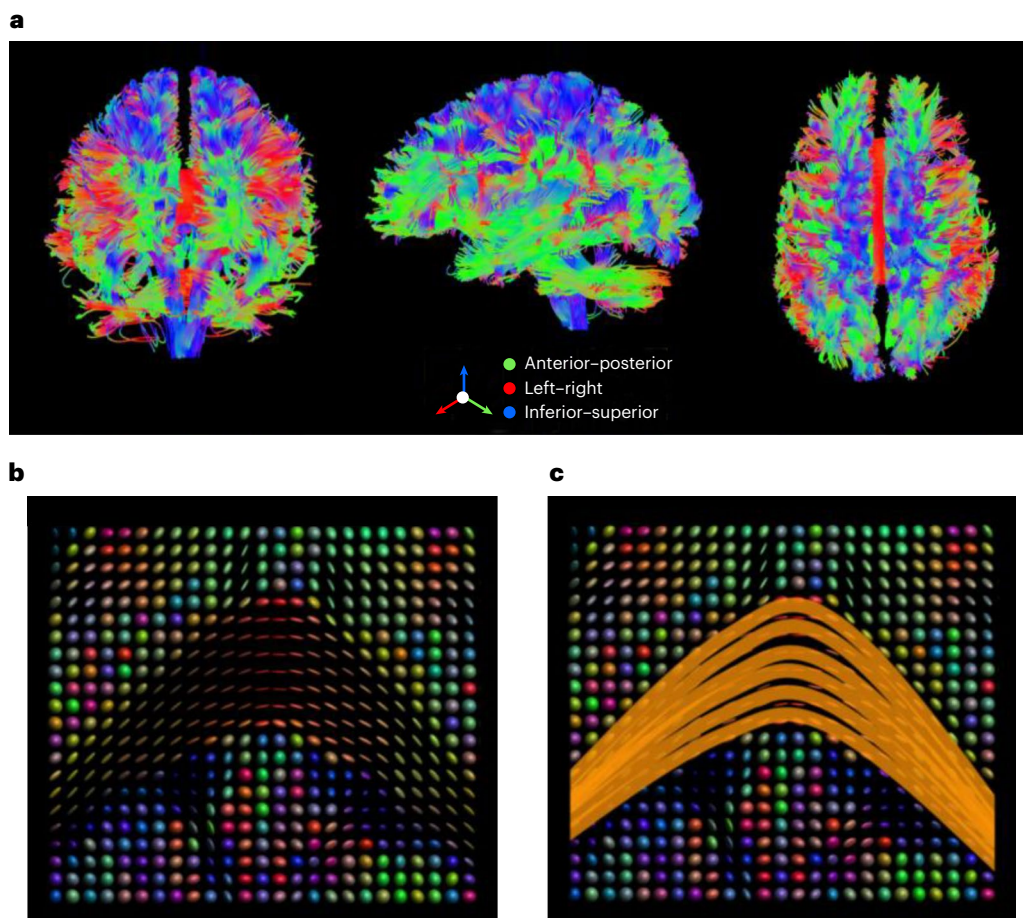


Fig. 5 | Tractography. **a**, A tractogram representing tracks across the entire brain color coded according to diffusion directions seen from different viewpoints: coronal (left column), sagittal (mid column) and axial (right column).

b,c, Tractography estimation, starting from a tensor field across an ROI (**b**) and ending in the streamline estimation of tracks across the region (**c**).

(ODF), also known as fiber ODF (fODF) or fiber orientation distribution (FOD). All three terms describe the directionality of complex fiber architecture using a probability density function that quantifies the distribution in correspondence with set orientations on a voxel-wise basis^{67–70}. All tractography algorithms use dMRI to reveal trajectories of WM fibers across the brain using reconstruction techniques for streamline estimation based on principal diffusion directions. However, fiber tracking algorithms apply different approaches to infer the architecture of WM⁵⁶:

- Deterministic tractography: delineates WM pathways using line propagation algorithms. The line propagation process starts with the identification of a suitable starting seed point, followed by propagation along the estimated tract orientation and ending when tract termination criteria are met. The main limitation of deterministic fiber tracking is that it provides a single estimate of WM tracts from each seed point, without any indication of the likelihood or confidence in the path estimation
- Probabilistic tractography: designed to deal with the limitation of deterministic fiber tracking by assigning likelihood to paths using a probability distribution. These algorithms consider that noise in dMRI can lead to errors in the line propagation, which in turn can have a notable cumulative effect on the resulting reconstructed tract. Nevertheless, probabilistic fiber tracking is not considered more precise than deterministic fiber tracking, since it uses the same basic methods and therefore suffers from similar setbacks. Some probabilistic fiber tracking algorithms use greedy

optimization techniques on a local scale that result in prolonged processing, while others utilize random direction selection from the ODF and result in increased efficiency

- Global tractography: a class of tractography algorithms that differs conceptually and methodologically from streamline tractography. Global tractography involves finding the full track configuration that best explains the measured DWI data using greedy algorithms to reconstruct all fibers simultaneously. Every fiber segment is considered a model parameter that contributes as a single isotropic Gaussian model. These parameters are then optimized to form longer chains of segments, or fiber tracks, with overall low curvature. The main limitation of this approach lies in the greedy, time-consuming nature of this group of algorithms. Even so, global tractography has been shown to better deal with noisy datasets and reconstruct complex fiber anatomy more accurately, resulting in a tractogram with density values that relate more directly to the measured data⁷¹.

The approaches discussed above involve whole-brain tractography for the inference of structural brain connectivity. Other approaches include region of interest (ROI)-based tractography, which is not designed for connectivity but rather for dedicated fiber structures. ROI-based tractography focuses on tracking only chosen fiber groups, such as the optic radiation or the corticospinal tract. Its seeding and evaluation methods differ accordingly, depending on the imaging needs, as well as the location and anatomy of the examined fiber structure⁷².

Advanced techniques for tractography

Despite the conceptual and methodological limitations of fiber tracking (discussed above), important progress is continuously being made in the acquisition, processing, modeling, analysis and visualization of fiber tracking. A recent fiber tracking study⁷³ has presented a previously unknown bilateral fiber tract in the frontal region of the brain named the superoanterior fasciculus, similar in shape to the anterior part of the cingulum bundle but more frontally located. The study demonstrates consistency in the previously undocumented superoanterior fasciculus pathway across subjects, different dMRI datasets and various processing pipelines⁷³.

HARDI is often used as an advanced dMRI scan protocol for better capturing crossing fibers by using high resolution of the *q*-space^{64,65} (Fig. 4b–e). Use of high angular resolution with multiple *b*-value shells creates images with higher definition that necessitate non-DTI reconstruction techniques, such as ball-and-stick (BAS) and constrained spherical deconvolution (CSD):

- The BAS model: a popular probabilistic approach to tractography that uses geometric features of the HARDI signal to model axons as cylinders with a single radius and impermeable membrane, while assuming isotropic diffusion outside the axons. BAS deconstructs the signal into a fully isotropic compartment (ball) and a fully anisotropic one (stick). Similar models have since been proposed as expansions of the BAS model, such as the ball-and-racket model⁷⁴
- CSD: another popular approach to tractography based on a mathematical operation called spherical deconvolution, which generates a third function from two existing ones. CSD expresses the HARDI signal as the convolution operation over spherical coordinates of two functions: the signal of a single oriented set of fibers, or the response function, and the FOD. The result is an estimation of the distribution of fiber orientations in each voxel⁷⁵

In recent applications, tractography errors are substantially reduced by seeding the tracts from the intersection between the WM and GM surfaces^{76,77}. Other modern applications attempt to use WM atlases and artificial intelligence to find logical, knowledge-based tracts. However, these approaches are still in their infancy^{78,79}.

Tractography criteria. Regardless of the approach, all tractography techniques use dMRI to reconstruct fiber track streamlines. To avoid error propagation, the streamlines flow and stop according to several criteria⁷⁹:

- Smoothness criterion: a curvature threshold that limits the maximal possible bend in streamline estimation, used for avoiding estimation of overly curved and inaccurate streamlines and overcoming crossing fibers
- Anisotropy criterion: a threshold that limits the streamline propagation into isotropic regions, used for avoiding streamline estimation inside regions with no dominant direction, where the vector field is irrelevant
- Anatomical criteria: a set of criteria based on prior knowledge of the expected fiber tract anatomy, for example, regions with expected GM content¹⁹

For tractography applications in connectomics, seeding and termination criteria are particularly important. Termination criteria involve the various specifications and thresholds for determining the streamline end points, including the abovementioned smoothness, anisotropy and anatomical criteria. Seeding criteria on the other hand involve the number, density and locations of seeds or start points from which the streamline flow propagates.

Tractogram evaluation. Evaluating the accuracy of a tractogram involves comparison of the patterns of cortical connectivity to a ground truth of expected values. This comparison of connections (or lack thereof) between pairs of regions, involves the use of a confusion

matrix, which summarizes the performance of a classification model using four parameters: true positive (valid connections), true negative (no connection where none was expected), false positive (connection where none was expected) and false negative (no connection where one was expected). Additional parameters, such as sensitivity and specificity, can be extracted from these values. One such tool for evaluating the accuracy of different variations of tractography is the Tractometer, an online tool that measures the effect of different imaging and processing choices on the resulting tractogram^{80,81}. Yet most of the evaluation is commonly done subjectively, by a neuroanatomist that can indicate if a tract is logical or not. For example, when seeking a specific connection (e.g., the corpus callosum), an iterative, manual, procedure of removing spurious streamlines is done until the expected neuroanatomical presentation is met. While such evaluations cannot be done on large datasets and for all reconstructed fibers, it is important for anyone who wishes to use tractography to undergo this experience in relation to known anatomy to understand the pitfalls and magnitude of false connections.

Errors and limitations of tractography

Despite the many advantages of tractography, this process also exhibits several methodological errors and limitations. One fundamental limitation of tractography involves the strong effect of the choice of methodology. The choice of methodology and tractography algorithm has a strong effect on the accuracy of the resulting tractogram, revealing a tradeoff between sensitivity and specificity⁷¹. The following are some of the major challenges of tractography today:

- Difficulty reconstructing complex geometry: one of the most challenging issues in tractography involves estimating intricate fiber architecture, such as overlapping, branching and crossing pathways. Connectivity inference from local orientation fields becomes increasingly error prone when the pathways involve more intricate geometries due to averaging of values within a single voxel (PVE). Miscalculations of crossing fibers are often evident in association fibers in locations such as the intersection of the forceps minor with the corona radiata and the intersection of the fanning of the corticospinal tracts with the superior longitudinal fasciculus. Some solutions have been offered for crossing fibers on a local scale, but the problem persists on the global scale⁵⁸. The bottleneck problem, possibly an even greater reconstruction challenge, involves disentangling fibers that converge within a voxel (or group of voxels) before branching out into differing directions. Bottlenecks are common in regions such as deep within WM in the occipital lobe, in the anterior–posterior direction, including multiple individual WM fasciculi with similar orientations^{18,82}
- Difficulty delineating track boundaries: as axons can split and merge at any point along the fiber tract, tractography experiences challenges accurately determining the boundaries of a streamline. The main cause for termination miscalculations is the PVE associated with the voxel-wise approach. In this case, PVE involves not only cases in which WM fibers with different orientations appear in the same voxel, but also cases in which both WM and GM appear in a single voxel. These challenges are experienced in GM both laterally, across the cortical folding (sulco-gyrus bias), and radially, with respect to the laminar start and end of a streamline. This difficulty has also resulted in a biased representation of the cerebral cortex as a single homogeneous unit that ignores its microstructural composition⁸³. Additionally, it raises questions regarding the lack of a straightforward definition of a tract, which further exacerbates the inherent difficulty of validating *in vivo* imaging with no clear-cut ground truth^{71,84–87}
- Difficulties reconstructing very ‘strong’ and very small tracts: even when using high-resolution images, tractography often results in high false positive rates involving tractograms that contain more

invalid (illogical and/or disconnected) than valid fiber bundles. One of the main causes for this issue is the increasingly high certainty that fiber tracking algorithms tend to assign to strong tracts. Simultaneously, tractography experiences high false negative rates due to difficulties reconstructing very small tracts with diameters of 2 mm or less, such as the anterior commissure^{3,18,67,71,82,83,85,86}.

Structural networks

The main challenge of connectivity research is adequately representing the tractography results so they can be quantified and compared both within and across subjects. Over the past decade, the use of graph theory tools has become state of the art in brain connectivity analysis. A diagram of brain connectivity is typically modeled as a network graph, which is a mathematical structure that uses graph edges to model interactions between different components, represented as graph nodes⁷⁹. In a brain network, nodes signify cortical (or subcortical) regions and edges signify connections between pairs of regions. A network graph is summarized as a list of nodes and a corresponding list of edges. A node is a labeled vertex or point in space with 3D coordinates. An edge is a line connecting two nodes with a weighted value of either absolute or relative strengths, or an unweighted binary value. An edge can be undirected or directed.

Currently, the field of connectomics encompasses three types of brain connectivity: structural, functional and effective connectivity, each explored using different MRI modalities and modeled as a different type of network graph¹. Structural connectivity represents anatomical links, or fiber bundles, connecting different cortical regions. The structural connectome is measured using dMRI tractography and is therefore modeled as an undirected and weighted network graph, in which weights represent ‘strengths’ of anatomical links⁸⁵.

Network construction. Node selection: a brain network node is expected to be spatially constrained and to exhibit some intrinsic consistency, such as within-node similarity in cytoarchitecture or function. Simultaneously, a node is expected to exhibit some extrinsic differentiation or variability in connections between nodes. Besides these general guidelines, there is no consensus on an optimal definition of these brain network units. The way the nodes are defined is a result of the topology we seek to explore, focusing on either long-range or fine-grained connections. On the one hand, choosing small nodes that include individual MRI voxels will result in a very detailed network with many nodes and edges, but it may also include inaccuracies related to resolution that can cloud more dominant connectivity patterns. On the other hand, choosing large units will result in a seemingly less detailed network with fewer nodes and edges, but it may also better showcase more dominant connectivity patterns^{17,19}. For example, the former is better suited for exploring fine-grained variations in heteromodal association systems, while the latter is better suited for intersubject comparisons. There are two basic rules of thumb for node selection:

- Full topological coverage: to get a whole-brain structural connectome, the nodes must cover all cortical regions and preferably subcortical regions as well
- No topological overlap: to get a true representation of the connections of each network node, overlap between cortical regions must be avoided

Atlases, or cortical parcellations, are the lens through which the patterns of cortical connectivity are examined. A wide variety of atlases exists, including some of the following: cytoarchitecture⁸⁸, myelo-architecture⁸⁹, anatomical⁹⁰, probabilistic⁹¹, random⁹², functional⁹³, data-driven^{94,95}, voxel-based⁹⁶ and multimodal atlases⁹⁷. An additional parcellation option involves blind source separation based on spatial

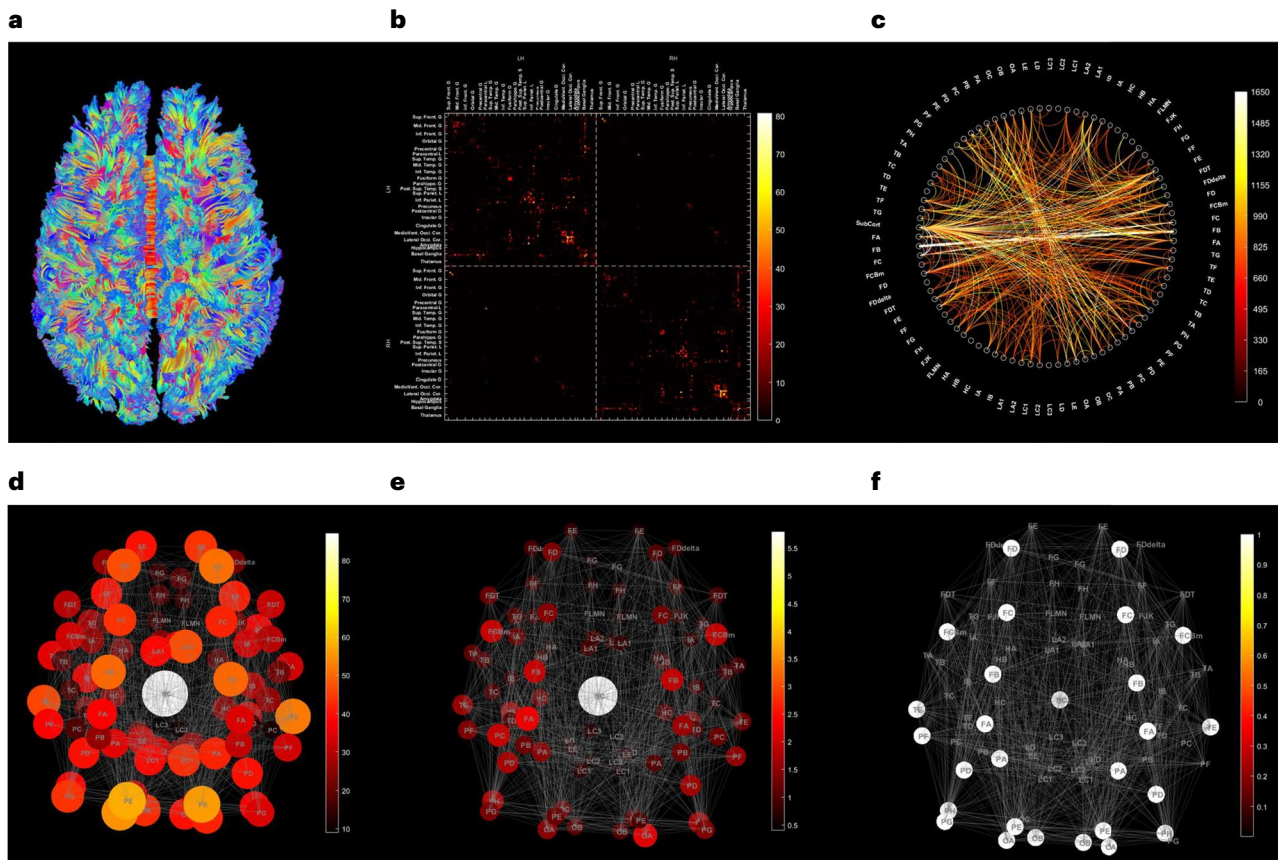


Fig. 6 | Networks visualizations and measures. **a–c**, Network visualizations (top): whole-brain tractogram (**a**), connectivity matrix across Brainnetome atlas regions (**b**) and circular graph across Von Economo-Koskinas atlas regions (**c**). **d–f**, Network measures (bottom): three different local network measures,

including degree (**d**), clustering coefficient (**e**) and core/periphery (**f**). These three network measures represent exemplary measures of centrality, segregation and hubs, respectively. All network and images seen from a superior view.

Table 3 | Tools for analysis and visualization of brain networks

Toolbox	Details	Refs.
1 Brain Connectivity Toolbox	A Python and MATLAB toolbox for both analysis and visualization of brain networks. Contains a collection of complex network measures and neuroanatomical connectivity datasets (https://sites.google.com/site/bctnet/)	7
2 MRtrix3	An open-source Python toolbox for both analysis and visualization of brain networks (https://www.mrtrix.org/)	9
3 DIPY (Diffusion Imaging In Python)	A python library for multidimensional imaging. Contains a variety of medical imaging tools (for signal processing, machine learning, etc.), alongside specialized tools for computational anatomy, including dMRI and structural imaging (https://dipy.org/)	112
4 NetworkX	A Python toolbox for the creation, manipulation, and study of the structure, dynamics, and functions of complex network. Designed for networks in general, also applicable for brain networks (https://networkx.org/)	113
5 ExploreDTI	A MATLAB toolbox for DTI analysis that enables both analysis and visualization of brain networks. Designed for exploratory DTI and fiber tractography (https://www.exploredti.com/)	8
6 muxViz	A platform developed using R and GNU Octave that provides customizable graphic options to analyze and visualize a variety of multilayered networks (https://muxviz.wordpress.com/)	114
7 Circos	An advanced tool for network visualization as circular graphs. Written in Perl and deployable wherever Perl is available. Originally conceived for visualizing genomic data, it has been since used in other fields, including connectomics (http://circos.ca/)	115
8 Circular graph visualization: (circularGraph, Circular-Connectome)	Two MATLAB tools for visualization of brain networks as circular graphs (https://github.com/paul-kassebaum-mathworks/circularGraph) (https://github.com/ittais/Circular-Connectome)	116

independence of nodes⁹⁸. This data-driven parcellation requires pre-specification of the number of regions (or nodes) based on homogeneity, accuracy, reproducibility or stability of the network. Preferably, for better intersubject comparison, brain regions should be delineated using data from both structural and functional connectivity across both modalities and individuals⁸⁵.

Edge selection: regarding edge definition, the weight of an edge connecting two nodes in a structural connectome is often represented by the number of streamlines connecting the two corresponding regions in the tractogram. The use of the number of streamlines as weights is biased due to the error-prone nature of this methodology when it comes to estimating complex streamlines and streamline endpoints (see the section on ‘Errors and limitations of tractography’). Furthermore, the use of the number of streamlines as edges is also inherently limited by the lack of additional streamline features, besides their presence or absence. Preferably, edges in a structural connectome should accurately represent all the features of axonal connections that influence the propagation of action potentials, including axon myelination, length, size and density. These microstructural features are missing in the use of the number of streamlines as edges and are more relevant to measures such as FA. However, despite its sensitivity to axonal microstructure, FA is also prone to PVE and errors in estimation of axonal dispersion⁹⁹.

This issue, also known as the track-count bias, is tackled using various techniques for reweighting the edges in the network in a more biologically meaningful way⁷. Some techniques reweight the edges based on normalized axon diameters, using methods such as COMMIT and AxSI (see the section on ‘The parametric approach: biophysical models’)^{53,62}. Other techniques aim to increase the biological relevance of the edges by filtering out edges through methods such as spherical-deconvolution informed filtering of tractograms^{100,101}. Linear fascicle evaluation is another tract-filtering method that assigns weights according to the contribution of each tract to predicting the diffusion data^{17,53,102}.

To analyze the resulting structural networks, weighted edges can be normalized, binarized or left as-is with the existing range of streamlines. Threshold selection is particularly important in densely connected networks, but it can also be arbitrary (i.e., percentile, average, etc.). While weighted edges are assumed to contain more information regarding weak connections, binary edges are relatively simpler to characterize and compare between subjects^{17,19}.

Network analysis. The benefit of modeling brain connectivity as a network graph lies in the applicability of graph theory techniques for analyzing structural patterns of network graphs. Gaining a better understanding of the structure and function of a brain network necessitates a review of its topology. Brain topology can be extracted using network analysis tools. Complex network analysis deals with real-life networks that are both large and complex, unlike uniformly random or ordered networks. Complex networks exhibit nontrivial topological features that do not occur in simple networks, such as random graphs. Brain networks exhibit these nontrivial features in their node measures. For instance, a heavy tail in degree distribution, a high clustering coefficient, and a community and hierarchy structure (for definitions, see Supplementary Table 1). In addition, graph theory provides a set of tools for conducting simple and efficient intersubject comparisons of different measures. Network measures include those evaluated per node on a local scale (subnetwork), and those evaluated for the entire network on a global scale. Measures of brain connectivity can generally be classified into three categories⁷: measures of centrality, which signify the importance of individual nodes; measures of segregation, which signify the ability to conduct specialized processing in clusters of nodes; and measures of integration, which signify the ability to combine information across clusters of nodes.

Small-worldness is a characteristic of networks that reconciles the demand for segregation into processing clusters with the demand for integration of information across the network^{7,103}. Small-world networks hold a balance between segregation into specialized processing clusters and integration of information across these clusters. These networks exhibit high efficiency, caused by a low value of mean shortest path, that approximately follows a logarithmic law. Brain networks exhibit not only ‘small worldness’, but also a ‘rich-club organization’, a phenomenon that involves the tendency of high-degree nodes to also be highly interconnected. Nodes that are part of the ‘rich club’ are considered network hubs^{103,104}. For a list of neurobiologically meaningful network measures, including global and local measures of centrality, segregation, integration and hubs, see Supplementary Table 1 (ref. 7). For a visualization of various measures across a brain network, see Fig. 6d–f. Additional approaches to exploring structural connectivity include data-driven clustering and modularity, as well as using cortical gradients to map trends in connectivity. It is expected that modularity will play a critical role in defining network topologies in future neuroimaging studies^{105,106}.

Network visualization. An additional benefit of modeling brain connectivity as a network graph lies in the ability to use a variety of existing tools for advanced network visualization. Modeling brain networks as network graphs results in two lists: a list of network nodes (N) with spatial locations (x, y, z), and a list of network edges (M) connecting pairs of nodes (node A, node B). These networks can be visualized in several different ways (Fig. 6a–c):

- **Connectivity matrix:** an $N \times N$ matrix C in which rows and columns represent network nodes, and individual values $C(i,j)$ represent connections strengths between nodes i and j . Undirected networks are visualized as symmetric connectivity matrices, and directed networks are visualized as asymmetric matrices
- **Network graph:** the classic representation of a network, in which nodes are represented spatially as spheres with locations (x, y, z) and edges are represented as lines connecting pairs of nodes. Edges in undirected networks are visualized as lines, and in directed networks they are visualized as arrows
- **Circular graph:** a circular visualization of a network, in which a circle is divided into sectors, representing network nodes, that are connected by curved lines, representing network edges

In all the abovementioned ways, edge weights are often visualized by the width and color of the connections. For a list of several useful toolboxes for both analysis and visualization of brain networks, see Table 3.

Concluding remarks

dMRI provides opportunities to study brain physiology by measuring microstructural changes following neuroplasticity, as well as visualizing and quantifying information transfer in the brain through connectivity analysis noninvasively. We anticipate that dMRI will increasingly be used to complement fMRI studies in translational brain studies.

References

- Park, H. J. & Friston, K. Structural and functional brain networks: from connections to cognition. *Science* **342**, 1238411 (2013).
- Van Essen, D. C. et al. The WU-Minn human connectome project: an overview. *Neuroimage* **80**, 62–79 (2013).
- Jbabdi, S. & Johansen-Berg, H. Tractography: where do we go from here? *Brain Connect.* **1**, 169–183 (2011).
- Van Essen, D. C. & Glasser, M. F. The human connectome project: progress and prospects. *Cerebrum* **2016**, cer-10-16 (2016).
- Jones, D. K. *Diffusion MRI: Theory, Methods, and Applications* (Oxford University Press, 2012).
- Dale, B. M., Brown, M. A. & Semelka, R. C. *MRI: Basic Principles and Applications* 5th edn. (Wiley-Blackwell, 2015).
- Rubinov, M. & Sporns, O. Complex network measures of brain connectivity: uses and interpretations. *Neuroimage* **52**, 1059–1069 (2010).
- Leemans, A., Jeurissen, B., Sijbers, J. & Jones, D. K. ExploreDTI: a graphical toolbox for processing, analyzing, and visualizing diffusion MR data. In *17th Annual Meeting of the International Society of Magnetic Resonance in Medicine* 3537 (ISMRM, 2009).
- Tournier, J. D. et al. Mrtrix3: A fast, flexible and open software framework for medical image processing and visualization. *Neuroimage* **202**, 116–137 (2019).
- Theaud, G., Houde, J. C., Rheault, A. B. F., Morency, F. & Descoteaux, M. TractoFlow: a robust, efficient and reproducible diffusion MRI pipeline leveraging Nextflow & Singularity. *Neuroimage* **218**, 116889 (2020).
- Cieslak, M. et al. QSIprep: an integrative platform for preprocessing and reconstructing diffusion MRI data. *Nat. Methods* **18**, 775–778 (2021).
- Cruces, R. R. et al. Micapipe: a pipeline for multimodal neuroimaging and connectome analysis. *Neuroimage* **263**, 119612 (2022).
- Assaf, Y. & Barazany, D. in *Advances in Magnetic Resonance Technology and Applications* Vol. 4 (eds. Cohi, Y. & Jezzard, P.) 157–173 (Academic Press, 2021).
- Johansen-Berg, H. & Behrens, T. E. J. *Diffusion MRI: From Quantitative Measurement to In vivo Neuroanatomy* 2nd edn. (Elsevier, 2014).
- Tavor, I., Hofstetter, S. & Assaf, Y. Micro-structural assessment of short term plasticity dynamics. *Neuroimage* **81**, 1–7 (2013).
- Assaf, Y. Imaging laminar structures in the gray matter with diffusion MRI. *Neuroimage* **197**, 677–688 (2019).
- Sotiroopoulos, S. N. & Zalesky, A. Building connectomes using diffusion MRI: why, how and but. *NMR Biomed.* **32**, e3752 (2019).
- Rheault, F., Poulin, P., Valcourt Caron, A., St-Onge, E. & Descoteaux, M. Common misconceptions, hidden biases and modern challenges of dMRI tractography. *J. Neural Eng.* **17**, 011001 (2020).
- Yeh, C. H., Jones, D. K., Liang, X., Descoteaux, M. & Connelly, A. Mapping structural connectivity using diffusion MRI: challenges and opportunities. *J. Magn. Reson. Imaging* **53**, 1666–1682 (2021).
- Helenius, J. et al. Diffusion-weighted MR imaging in normal human brains in various age groups. *Am. J. Neuroradiol.* **23**, 194–199 (2002).
- Schlaug, G., Siewert, B., Benfield, A., Edelman, R. R. & Warach, S. Time course of the apparent diffusion coefficient (ADC) abnormality in human stroke. *Neurology* **49**, 113–119 (1997).
- Kuroiwa, T. et al. Different apparent diffusion coefficient: water content correlations of gray and white matter during early ischemia. *Stroke* **29**, 859–865 (1998).
- van Everdingen, K. J., van der Grond, J., Kappelle, L. J., Ramos, L. M. P. & Mali, W. P. T. M. Diffusion-weighted magnetic resonance imaging in acute stroke. *Stroke* **29**, 1783–1790 (1998).
- Harkins, K. D., Galons, J. P., Secomb, T. W. & Trouard, T. P. Assessment of the effects of cellular tissue properties on ADC measurements by numerical simulation of water diffusion. *Magn. Reson. Med.* **62**, 1414–1422 (2009).
- Jose, J. M., Marques, P., Alves, V. & Nuno, S. A hitchhiker's guide to diffusion tensor imaging. *Front. Neurosci.* **7**, 1–14 (2013).
- Sener, R. N. Diffusion MRI: apparent diffusion coefficient (ADC) values in the normal brain and a classification of brain disorders based on ADC values. *Comput. Med. Imaging Graph.* **25**, 299–326 (2001).
- Barrio-Arranz, G., de Luis-García, R., Tristán-Vega, A., Martín-Fernández, M. & Ajá-Fernández, S. Impact of MR acquisition parameters on DTI scalar indexes: a tractography based approach. *PLoS ONE* **10**, e0137905 (2015).
- Assaf, Y., Johansen-Berg, H. & Thiebaut de Schotten, M. The role of diffusion MRI in neuroscience. *NMR Biomed.* **32**, e3762 (2019).
- Blumenfeld-Katzir, T., Pasternak, O., Dagan, M. & Assaf, Y. Diffusion MRI of structural brain plasticity induced by a learning and memory task. *PLoS ONE* **6**, e20678 (2011).
- Tavor, I., Botvinik-Nezer, R., Bernstein-Eliav, M., Tsarfaty, G. & Assaf, Y. Short-term plasticity following motor sequence learning revealed by diffusion magnetic resonance imaging. *Hum. Brain Mapp.* **41**, 442–452 (2020).
- Assaf, Y. New dimensions for brain mapping. *Science* **362**, 994–995 (2018).
- Sagi, Y. et al. Learning in the fast lane: new insights into neuroplasticity. *Neuron* **73**, 1195–1203 (2012).
- Hofstetter, S., Tavor, I., Tzur-Moryosef, S. & Assaf, Y. Short-term learning induces white matter plasticity in the fornix. *J. Neurosci.* **33**, 12844–12850 (2013).
- Hofstetter, S., Friedmann, N. & Assaf, Y. Rapid language-related plasticity: microstructural changes in the cortex after a short session of new word learning. *Brain Struct. Funct.* **222**, 1231–1241 (2017).

35. Henf, J., Grothe, M. J., Brueggen, K., Teipel, S. & Dyrba, M. Mean diffusivity in cortical gray matter in Alzheimer's disease: The importance of partial volume correction. *Neuroimage Clin.* **17**, 579–586 (2018).
36. Duncan, J. S. Imaging the brain's highways-diffusion tensor imaging in epilepsy. *Epilepsy Curr.* **8**, 85–89 (2008).
37. Szczepankiewicz, F. et al. Quantification of microscopic diffusion anisotropy disentangles effects of orientation dispersion from microstructure: applications in healthy volunteers and in brain tumors. *Neuroimage* **104**, 241–252 (2015).
38. Kaden, E., Kelm, N. D., Carson, R. P., Does, M. D. & Alexander, D. C. Multi-compartment microscopic diffusion imaging. *Neuroimage* **139**, 346–359 (2016).
39. Henriques, R. N., Jespersen, S. N. & Shemesh, N. Microscopic anisotropy misestimation in spherical-mean single diffusion encoding MRI. *Magn. Reson. Med.* **81**, 3245–3261 (2019).
40. Magdoom, K. N., Avram, A. V., Sarlls, J. E., Dario, G. & Basser, P. J. A novel framework for in-vivo diffusion tensor distribution MRI of the human brain. *Neuroimage* **271**, 120003 (2023).
41. Stejskal, E. O. & Tanner, J. E. Spin diffusion measurements: spin echoes in the presence of time-dependent field gradient. *J. Chem. Phys.* **42**, 288–292 (1965).
42. Assaf, Y., Mayk, A. & Cohen, Y. Displacement imaging of spinal cord using q-space diffusion-weighted MRI. *Magn. Reson. Med.* **44**, 713–722 (2000).
43. Cohen, Y. & Assaf, Y. High *b*-value q-space analyzed diffusion-weighted MRS and MRI in neuronal tissues—a technical review. *NMR Biomed.* **15**, 516–542 (2002).
44. Jensen, H. J. & Helpern, J. A. MRI quantification of non-Gaussian water diffusion by kurtosis analysis. *NMR Biomed.* **23**, 698–710 (2010).
45. Steven, A. J., Zhuo, J. & Melhem, E. R. Diffusion kurtosis imaging: an emerging technique for evaluating the microstructural environment of the brain. *Am. J. Roentgenol.* **202**, W26–W33 (2014).
46. Henriques, R. N. et al. Diffusional kurtosis imaging in the diffusion imaging in Python project. *Front. Hum. Neurosci.* **15**, 675433 (2021).
47. Assaf, Y. & Basser, P. J. Composite hindered and restricted model of diffusion (CHARMED) MR imaging of the human brain. *Neuroimage* **27**, 48–58 (2005).
48. Zhang, H., Schneider, T., Wheeler-Kingshott, C. A. & Alexander, D. C. NODDI: practical in vivo neurite orientation dispersion and density imaging of the human brain. *Neuroimage* **61**, 1000–1016 (2012).
49. Scherrer, B. et al. Characterizing brain tissue by assessment of the distribution of anisotropic microstructural environments in diffusion-compartment imaging (DIAMOND). *Magn. Reson. Med.* **76**, 963–977 (2016).
50. Assaf, Y., Blumenfeld-Katzir, T., Yovel, Y. & Basser, P. J. AxCaliber: a method for measuring axon diameter distribution from diffusion MRI. *Mag. Reson. Med.* **59**, 1347–1354 (2008).
51. Barazany, D., Basser, P. J. & Assaf, Y. In vivo measurement of axon diameter distribution in the corpus callosum of rat brain. *Brain* **132**, 1210–1220 (2009).
52. Assaf, Y. et al. The CONNECT project: combining macro- and micro-structure. *Neuroimage* **80**, 273–282 (2013).
53. Daducci, A., Dal Palù, A., Lemkadem, A. & Thiran, J. P. COMMIT: convex optimization modeling for microstructure informed tractography. *IEEE Trans. Med. Imaging* **34**, 246–257 (2015).
54. Barakovic, M. et al. Bundle-specific axon diameter index as a new contrast to differentiate white matter tracts. *Front. Neurosci.* **15**, 646034 (2021).
55. Drakesmith, M. et al. Estimating axon conduction velocity in vivo from microstructural MRI. *Neuroimage* **203**, 116186 (2019).
56. Dyrby, T. B., Søgaard, L. V., Hall, M. G., Ptito, M. & Alexander, D. C. Contrast and stability of the axon diameter index from microstructure imaging with diffusion MRI. *Magn. Reson. Med.* **70**, 711–721 (2013).
57. Harkins, K. D., Beaulieu, C., Xu, J., Gore, J. C. & Does, M. D. A simple estimate of axon size with diffusion MRI. *Neuroimage* **227**, 117619 (2021).
58. Daducci, A. et al. Accelerated Microstructure Imaging via Convex Optimization (AMICO) from diffusion MRI data. *Neuroimage* **15**, 32–44 (2015).
59. Romascano, D. et al. ActiveAxADD: toward non-parametric and orientationally invariant axon diameter distribution mapping using PGSE. *Magn. Reson. Med.* **83**, 2322–2330 (2020).
60. Veraart, J. et al. Noninvasive quantification of axon radii using diffusion MRI. *eLife* **9**, e49855 (2020).
61. Horowitz, A. et al. In vivo correlation between axon diameter and conduction velocity in the human brain. *Brain Struct. Funct.* **220**, 1777–1788 (2015).
62. Gast, H. et al. A method for in-vivo mapping of axonal diameter distributions in the human brain using diffusion-based axonal spectrum imaging (AxSI). *Neuroinformatics* **21**, 469–482 (2023).
63. Sepehrband, F., Alexander, D. C., Kurniawan, N. D., Reutens, D. C. & Yang, Z. Towards higher sensitivity and stability of axon diameter estimation with diffusion-weighted MRI. *NMR Biomed.* **29**, 293–308 (2016).
64. Heidemann, R. M., Anwander, A., Feiweier, T., Knösche, T. R. & Turner, R. *k*-space and *q*-space: combining ultra-high spatial and angular resolution in diffusion imaging using ZOOPPA at 7 T. *Neuroimage* **60**, 967–978 (2012).
65. Tournier, J. D., Calamante, F. & Connelly, A. Determination of the appropriate *b* value and number of gradient directions for high-angular-resolution diffusion-weighted imaging. *NMR Biomed.* **26**, 1775–1786 (2013).
66. Wakana, S., Jiang, H., Nagae-Poetscher, L. M., van Zijl, P. C. & Mori, S. Fiber tract-based atlas of human white matter anatomy. *Radiology* **230**, 77–87 (2004).
67. Fillard, P. et al. Quantitative evaluation of 10 tractography algorithms on a realistic diffusion MR phantom. *Neuroimage* **56**, 220–234 (2011).
68. Zhan, L. et al. For the Alzheimer's Disease Neuroimaging Initiative. Comparison of nine tractography algorithms for detecting abnormal structural brain networks in Alzheimer's disease. *Front. Aging Neurosci.* **7**, 48 (2015).
69. Poulin, P., Jörgens, D., Jodoin, P. M. & Descoteaux, M. Tractography and machine learning: Current state and open challenges. *Magn. Reson. Imaging* **64**, 37–48 (2019).
70. Poulin, P. et al. TractInferno—a large-scale, open-source, multi-site database for machine learning dMRI tractography. *Sci. Data* **9**, 725 (2022).
71. Maier-Hein, K. H. et al. The challenge of mapping the human connectome based on diffusion tractography. *Nat. Commun.* **8**, 1349 (2017).
72. Colon-Perez, L. M. et al. A majority rule approach for region-of-interest-guided streamline fiber tractography. *Brain Imaging Behav.* **10**, 1137–1147 (2016).
73. David, S. et al. The superoanterior fasciculus (SAF): a novel white matter pathway in the human brain? *Front. Neuroanat.* **13**, 24 (2019).
74. Sotropoulos, S. N., Behrens, T. E. & Jbabdi, S. Ball and rackets: inferring fiber fanning from diffusion-weighted MRI. *Neuroimage* **60**, 1412–1425 (2012).
75. Jeurissen, B., Tournier, J. D., Dhollander, T., Connelly, A. & Sijbers, J. Multi-tissue constrained spherical deconvolution for improved analysis of multi-shell diffusion MRI data. *Neuroimage* **103**, 411–426 (2014).

76. St-Onge, E., Al-Sharif, N., Girard, G., Theaud, G. & Descoteaux, M. Cortical surfaces integration with tractography for structural connectivity analysis. *Brain Connect.* **11**, 505–517 (2021).
77. Shastin, D. et al. Surface-based tracking for short association fibre tractography. *Neuroimage* **260**, 119423 (2022).
78. Mu, J., Xu, Q., Tian, J. & Liu, J. The effect of feature image on sensitivity of the statistical analysis in the pipeline of a tractography atlas-based analysis. *Sci. Rep.* **7**, 12669 (2017).
79. Hagmann, P. et al. Mapping human whole-brain structural networks with diffusion MRI. *PLoS ONE* **2**, e597 (2007).
80. Côté, M. A., Boré, A., Girard, G., Houde, J. C. & Descoteaux, M. Tractometer: online evaluation system for tractography. *Med. Image Comput. Comput. Assist. Interv.* **15**, 699–706 (2012).
81. Côté, M. A. et al. Tractometer: towards validation of tractography pipelines. *Med. Image Anal.* **17**, 844–857 (2013).
82. Schilling, K. G. et al. Prevalence of white matter pathways coming into a single white matter voxel orientation: the bottleneck issue in tractography. *Hum. Brain Mapp.* **43**, 1196–1213 (2022).
83. Shamir, I. & Assaf, Y. Expanding connectomics to the laminar level: a perspective. *Netw. Neurosci.* **7**, 377–388 (2023).
84. Bastiani, M., Shah, N. J., Goebel, R. & Roebroeck, A. Human cortical connectome reconstruction from diffusion weighted MRI: The effect of tractography algorithm. *Neuroimage* **62**, 1732–1749 (2012).
85. Jones, D. K., Knösche, T. R. & Turner, R. White matter integrity, fiber count, and other fallacies: The do's and don'ts of diffusion MRI. *Neuroimage* **73**, 239–254 (2013).
86. De Santis, S., Drakesmith, M., Bells, S., Assaf, Y. & Jones, D. K. Why diffusion tensor MRI does well only some of the time: variance and covariance of white matter tissue microstructure attributes in the living human brain. *Neuroimage* **89**, 35–44 (2014).
87. Jeurissen, B., Descoteaux, M., Mori, S. & Leemans, A. Diffusion MRI fiber tractography of the brain. *NMR Biomed.* **32**, e3785 (2019).
88. Brodmann, K. *Vergleichende Lokalisationslehre der Grosshirnrinde* (Johann Ambrosius, 1909).
89. Glasser, M. F. & Van Essen, D. C. Mapping human cortical areas in vivo based on myelin content as revealed by T1- and T2-weighted MRI. *J. Neurosci.* **31**, 11597–11616 (2011).
90. Desikan, R. S. et al. An automated labeling system for subdividing the human cerebral cortex on MRI scans into gyral based regions of interest. *Neuroimage* **31**, 968–980 (2006).
91. Eickhoff, S. B., Heim, S., Zilles, K. & Amunts, K. Testing anatomically specified hypotheses in functional imaging using cytoarchitectonic maps. *Neuroimage* **32**, 570–582 (2006).
92. Fornito, A., Zalesky, A. & Bullmore, E. Network scaling effects in graph analytic studies of human resting-state fMRI data. *Front. Syst. Neurosci.* **4**, 22 (2010).
93. Fornito, A., Harrison, B. J., Zalesky, A. & Simons, J. S. Competitive and cooperative dynamics of large-scale brain functional networks supporting recollection. *Proc. Natl Acad. Sci. USA* **109**, 12788–12793 (2012).
94. Yeo, B. T. et al. The organization of the human cerebral cortex estimated by intrinsic functional connectivity. *J. Neurophysiol.* **106**, 1125–1165 (2011).
95. Power, J. D. et al. Functional network organization of the human brain. *Neuron* **72**, 665–678 (2011).
96. van den Heuvel, M. P., Stam, C. J., Boersma, M. & Hulshoff Pol, H. E. Small-world and scale-free organization of voxel-based resting-state functional connectivity in the human brain. *Neuroimage* **43**, 528–539 (2008).
97. Glasser, M. et al. A multi-modal parcellation of human cerebral cortex. *Nature* **536**, 171–178 (2016).
98. Eickhoff, S. B., Yeo, B. T. T. & Genon, S. Imaging-based parcellations of the human brain. *Nat. Rev. Neurosci.* **19**, 672–686 (2018).
99. Craddock, R. C. et al. Imaging human connectomes at the macroscale. *Nat. Methods* **10**, 524–539 (2013).
100. Smith, R. E., Tournier, J. D., Calamante, F. & Connelly, A. SIFT: spherical-deconvolution informed filtering of tractograms. *Neuroimage* **67**, 298–312 (2013).
101. Smith, R. E., Tournier, J. D., Calamante, F. & Connelly, A. The effects of SIFT on the reproducibility and biological accuracy of the structural connectome. *Neuroimage* **104**, 253–265 (2015).
102. Pestilli, F., Yeatman, J. D., Rokem, A., Kay, K. N. & Wandell, B. A. Evaluation and statistical inference for human connectomes. *Nat. Methods* **11**, 1058–1063 (2014).
103. van den Heuvel, M. P. & Sporns, O. Rich-club organization of the human connectome. *J. Neurosci.* **31**, 15775–15786 (2011).
104. Wig, G. S. Segregated systems of human brain networks. *Trends Cogn. Sci.* **21**, 981–996 (2017).
105. Bernhardt, B. C., Smallwood, J., Keilholz, S. & Margulies, D. S. Gradients in brain organization. *Neuroimage* **251**, 1189872022 (2022).
106. Royer, J. et al. Cortical microstructural gradients capture memory network reorganization in temporal lobe epilepsy. *Brain* **146**, 3923–3937 (2023).
107. Jones, D. K. The effect of gradient sampling schemes on measures derived from diffusion tensor MRI: a Monte Carlo study. *Magn. Reson. Med.* **51**, 807–815 (2004).
108. Le Bihan, D. Diffusion/perfusion MR imaging of the brain: from structure to function. *Radiology* **177**, 328–329 (1990).
109. Le Bihan, D., Urayama, S. I., Aso, T., Hanakawa, T. & Fukuyama, H. Direct and fast detection of neuronal activation in the human brain with diffusion MRI. *Proc. Natl Acad. Sci. USA* **103**, 8263–8268 (2006).
110. Le Bihan, D. The ‘wet mind’: water and functional neuroimaging. *Phys. Med. Biol.* **52**, R57–R90 (2007).
111. Le Bihan, D. Diffusion, confusion and functional MRI. *Neuroimage* **62**, 1131–1136 (2012).
112. Garyfallidis, E. et al. Dipy, a library for the analysis of diffusion MRI data. *Front. Neuroinform.* **8**, 8 (2014).
113. Hagberg, A. A., Schult, D. A. & Swart, P. J. Exploring network structure, dynamics, and function using NetworkX. In *Proc. of the 7th Python in Science Conference (SciPy 2008)* (eds. Varoquaux, G., Vaught, T. & Millman, J.) 11–15 (2008).
114. De Domenico, M., Porter, M. A. & Arenas, A. MuxViz: a tool for multilayer analysis and visualization of networks. *J. Complex Netw.* **3**, 159–176 (2015).
115. Krzywinski, M. I. et al. Circos: an information aesthetic for comparative genomics. *Genome Res.* **19**, 1639–1645 (2009).
116. Shamir, I. & Assaf, Y. An MRI-based, data-driven model of cortical laminar connectivity. *Neuroinformatics* **19**, 205–218 (2021).
117. Shamir, I., Tomer, O., Krupnik, R. & Assaf, Y. Modelling the laminar connectome of the human brain. *Brain Struct. Funct.* **227**, 2153–2165 (2022).
118. Callaghan, P. T. *Principles of Nuclear Magnetic Resonance Microscopy* (Oxford Univ. Press, 1993).
119. Le Bihan, D. *Diffusion and Perfusion Magnetic Resonance Imaging: Applications to Functional MRI* (Raven Press, 1995).
120. Pierpaoli, C. & Basser, P. J. Toward a quantitative assessment of diffusion anisotropy. *Magn. Reson. Med.* **36**, 893–906 (1996).
121. Basser, P. J., Mattiello, J. & LeBihan, D. MR diffusion tensor spectroscopy and imaging. *Biophys. J.* **66**, 259–267 (1994).
122. Pierpaoli, C., Jezzard, P., Basser, P. J., Barnett, A. & Di Chiro, G. Diffusion tensor MR imaging of the human brain. *Radiology* **201**, 637–648 (1996).
123. Basser, P. J. & Pierpaoli, C. A simplified method to measure the diffusion tensor from seven MR images. *Magn. Reson. Med.* **39**, 928–934 (1998).
124. Tournier, J. D., Mori, S. & Leemans, A. Diffusion tensor imaging and beyond. *Magn. Reson. Med.* **65**, 1532–1556 (2011).

Competing interests

The authors declare no competing interests.

Additional information

Supplementary information The online version contains supplementary material available at
<https://doi.org/10.1038/s41596-024-01052-5>.

Correspondence and requests for materials should be addressed to Yaniv Assaf.

Reprints and permissions information is available at www.nature.com/reprints.

Publisher's note Springer Nature remains neutral with regard to jurisdictional claims in published maps and institutional affiliations.

Springer Nature or its licensor (e.g. a society or other partner) holds exclusive rights to this article under a publishing agreement with the author(s) or other rightsholder(s); author self-archiving of the accepted manuscript version of this article is solely governed by the terms of such publishing agreement and applicable law.

© Springer Nature Limited 2024